QUANTIFYING THE EFFECT OF PLASMA SOURCE ION IMPLANTATION (PSII) IN STEEL SAMPLES NEAR EDGES

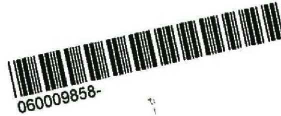

060009858-

North-West University
Mafikeng Campus Library

by

THULAGANYO PHILLIP SECHOGELA

516914570
251942482
118699625

LIBRARY
MAFIKENG CAMPUS
Call No.: TH 530.416
2006 -02- 15 SEC
Acc. No.: 06/00280
NORTH-WEST UNIVERSITY

A dissertation submitted in partial fulfillment of the requirements for the degree of Masters of Science in Applied Radiation, Science and Technology in the Faculty of Agriculture, Science and Technology at the University of North-West, Mafikeng-South Africa

2003

Acknowledgements

I would like to take this opportunity to thank my supervisor Dr C. Theron for his excellent supervision and advice. I would also like to thank everyone who offered assistance and encouragement during the research period.

Special thanks to Karl Springhorn, Lawrence Ashworth, Solomon Marsh and to the staff of Material Research Group of iThemba LABS for their assistance.

I am grateful also for encouragement I received form fellow postgraduates and I would like to thank them.

I am also grateful for financial support from the National Research Foundation (NRF) and the opportunity for using iThemba LABS facilities. I would also like to thank the University of North West through the Center for Applied Radiation Science and Technology (CARST) for granting me the opportunity to undertake this project.

Finally I would like to thank GOD almighty for His love and I would also like to thank my family for their support, encouragement and love.

ABSTRACT

Plasma source ion implantation was used to implant steel samples with nitrogen at energies of 20 keV and typical doses of $2x10^{16}$ ions/cm^2. Ion beam analytical techniques were then used to determine the depth profile of the implanted ions at various points between the center and the edge of the sample. The effect of pulse repetition rate was investigated; because it was assumed that an increase in the temperature by increasing the pulse frequency, nitrogen ions penetrate deeper into a sample. Rutherford backscattering spectrometry revealed that nitrogen ions were distributed to a depth of greater than at least 450 nm. For greater sensitivity the nuclear reaction $^{14}N(d,\alpha_0)^{12}C$ was used and the thickness of the iron nitride was found to be about 1.2 micrometers. The SIMNRA program was used to simulate the experimental spectra. The results are compared to simulated implantation profiles obtained with the monte-carlo code SRIM 2000. The nitrogen implantation varied across the sample.

Table of Contents

Chapter 1 1
Introduction 1
1.1 Motivation of the study 2
1.1.1 Significance of research 2
1.1.2 Scope of investigation 3
1.2 Thesis structure 4
Chapter 2 5
Surface modification techniques 5
Introduction 5
2.1 Surface coating techniques 5
2.1.1 Physical Vapour Deposition (PVD) 5
2.1.2 Chemical Vapour Deposition (CVD) 6
2.2 Surface modification 7
2.2.1 Heat treatment 7
2.2.2 Gas nitriding 7
2.3 Ion implantation 8
2.4 Ion implantation process 10
2.4.1 Sputtering 10
2.4.2 Secondary electron emission 11
2.4.3 Retained dose 12
2.4.4 Plasma formation 13
2.4.5 Ionization cross-section and mean-free path 14
2.4.6 Primary electron current limitations 16
2.4.6.1 Space charge limited emission 16
2.4.6.2 Temperature limited emission 16
2.4.7 Temperature versus space charge limitations 17
2.4.8 Sheath theory 17

Chapter 3 21
Experimental equipments and Analytical techniques background 21
3.1 Plan view 21
3.2 PSII features 22
3.2.1 Main chamber 22
3.2.2 Vacuum pumping system 25
3.2.3 Plasma generation 25
3.2.4 Working gas supply 25
3.2.5 Pulse generator 26
3.2.6 Diagnostics 27

3.2.7 Oscilloscope....28
3.3 Stopping and Ranges of Ions in Matter....28
3.4 Sample preparation....30
3.5 Target insertion....30
3.6 Netlab Software....31
3.6.1 Experimental application window....32
3.6.2 Implantation control window....33
3.7 Analytical techniques....34
3.8 General theory....34
3.8.1 Kinematic factor....35
3.8.2 Stopping power....36
3.8.3 Stopping in compounds....37
3.8.4 Evaluation of energy loss....37
3.8.5 Cross-section....38
3.8.6 Rutherford cross-section....38
3.8.7 Non-Rutherford cross-section....40
3.8.8 Nuclear reactions kinetics....40
3.8.9 Straggling....42
3.4.10 Nuclear reaction analysis....42

Chapter 4....44
4.1 Introduction....44
4.2 Sample geometry and treatment specification....45
4.3 Investigation of dose distribution....46
4.3.1 RBS measurements....46
4.3.2 NRA measurements....49
4.3.3 Distribution profile....51
4.4 The effect of pulse repetition rate....54
4.4.1 RBS measurements for sample P_2 and P_3....54
4.4.2 NRA measurements for sample P_2 and P_3....55
Chapter 5....57
5.1 Conclusion....57
5.2 Summary....58
5.3 Future work....59
Appendix A....60
A.1 Sputtering....60
A.1.1 Deposited energy....61
A.1.2 Sputtering yield....61
A.2 Semi-empirical formula for sputtering of single elemental targets....62
A.3 Sputtering at glancing angles....64
A.4 Ion implantation and the steady state condition....65
A.5 Sputtering of alloys and Compounds....66
A.5.1 Preferential sputtering....67
A.5.2 Composition changes....68
A.5.3 Composition depth profiles....68
A.6 High dose ion implantation....68

A.7 Factors that influence concentration in high dose implantation........................70
A.8 Sputtering spike..71

Appendix B 74
Sheath theory..74
B.1 Time scales..74
B.2 Dimensionless co-ordinates..75
B.3 The initial plasma sheath..76
B.4 Sheath evolution..78

Appendix C 81
Constants and formula..81
Table C.1 Physical constants..81
Table C.2 Lengths..81
Table C.3 Frequencies..82
Table C.4 Current density..83

References 84

List of Symbols

γ_{SE}	Secondary Electron Emission Coefficient
n_n	Neutral Gas Density (cm^{-3})
n_e	Electron Density (cm^{-3})
n_i	Ion Density (kg)
λ_m	Mean free path for collisions (m)
λ_D	Debye Length (m)
T_e	Electron Temperature (eV)
T_i	Ion Temperature (eV)
ϕ	Potential (V)
ϕ_f	Floating Potential (V)
ϕ_p	Plasma potential (V)
ε_0	Permittivity of free space ($C^2.N^{-1}.m^{-2}$)
ω_{pe}	Electron plasma frequency (Hz)
ω_{pi}	Ion plasma frequency (Hz)
τ_{pe}	Electron plasma period (s)
τ_{pi}	Ion plasma period (s)
τ_{pulse}	Pulse width (s)
m	Mass of electron
M	Mass of ion
e	Elementary charge (1.6×10^{-19} A-s)

List of Abbreviations

AES	Auger Electron Spectrometry
CVD	Chemical Vapour Deposition
ERDA	Elastic Recoil Detection Analysis
IBAD	Ion-Beam-Assisted Deposition
IBED	Ion-Beam-Enhanced Deposition
NRA	Nuclear Reaction Analysis
PIII	Plasma Immersion Ion Implantation
PIXE	Particle Induced X- ray Emission
PSII	Plasma Source Ion Implantation
PVD	Physical Vapour Deposition
RUP	Rossendorfer Universal Pulsegenerator
RBS	Rutherford Backscattering Spectrometry
SRIM	Stopping and Range of Ions in Matter
SPC	Solid Pole Cyclotron
SSC	Separated Sector Cyclotron

Chapter 1

Introduction

Plasma source ion implantation (PSII) or Plasma ion immersion implantation (PIII) [Bog02] is a relatively new technology developed in the 80's and open for research in the material technology [Con87]. Investigations in the past reveal that PSII/PIII technique is the better way for surface modification. This technique has gained increased interest for various applications such as in metal and semiconductor technology [Bri02]. In the past few years investigations showed that in lateral implantation, dose measurements of PIII non-planar target, there is a depletion of ions along the sample from center along the sample from the center to the edge caused by misalignment of the electrical field lines and the ions trajectories [Hart96]. Zeng et al. [Zeng99] carried out an investigation on the inner races of bearings to determine dose uniformity. They found that maximum ion dose was not in the middle or bottom of the arc groove. However, they are slightly displaced towards the side of the sample plate if the bearing were laid horizontally on the sample stage, the investigation combined both experimental (AES technique for nitrogen depth profile) and theoretical simulation results. A recent study [Liz02] of the biocompatibility improvement of NiTi with functionally graded surface revealed that ion implantation with oxygen alters the surface structure, composition and morphology of NiTi and this has implications for corrosion resistance and wear resistance. Wear corrosion resistance is an important factor for medical device applications and was substantially improved by Plasma source ion implantation.

1.1 Motivation of the study

1.1.1 Significance of research

iThemba LABS formerly known as the National Accelerator Center, is situated in Faure about 30 kilometers from Cape Town. It is a multidisciplinary scientific research laboratory administered by the National Research Foundation (NRF) and provides facilities for:

- Basic and applied research using particle beams,
- Particle radiotherapy for the treatment of cancer and
- The supply of accelerator–produced radioactive isotopes for nuclear medicine and research.

Activities are based around four accelerators. The large k=200 Separated Sector Cyclotron (SSC) accelerates protons to energies of 200 MeV. Charged particles are pre-accelerated to the SSC by the two-injector cyclotrons, capable of providing intense beams of light ions (SPC1) and the other beams of polarized light ions (SPC2). The fourth accelerator at iThemba LABS is a 6 MV Van de Graaff accelerator.

This study is based on implanting materials with nitrogen using the plasma source ion implantation (PSII) facility situated on the first floor of the Materials Research Group (MRG) building. It was designed and constructed for use by the MRG with specific application relevant to South African industry [Mey01]. The iThemba LABS PSII facility can be used to implant material of complex geometry like knee joint femoral, hip joint femoral heads [Che91]. The facility can be utilized even for orthopedic prostheses, which are made harder and more wear resistant by ion implantation into

the articulating surfaces [Chu02]. PSII facility can be used to implant material with a desired element, for example:

- Implanting Ti-6-Al-4-V with iridium to improve resistance to corrosion and
- Implanting Ti with nitrogen to reduce wear.

1.1.2 Scope of investigation

The study is based on surface modification of a material such as mild steel. It is essential then to investigate the dose across the center of the sample and to the edge. Out of this investigation conclusion will be drawn on how dose is distributed, whether the nitrogen ions are uniformly distributed into the sample or not, because it is important for industrial materials to be uniformly modified to avoid degradation from particular area to the other. Some of industrial materials e.g. drill bits, screwdriver etc use edges, as essential areas to perform a task smoothly, therefore there's a need to investigate retained dose across the edge. The workpiece will be implanted with nitrogen using PSII and nuclear reaction analysis will be employed using $^{14}N(d,\alpha_0)^{12}C$ as a base for analysis. The effect of pulse repetition rate when biasing the workpiece by high negative voltage will be investigated. This is done in order to understand the effect of pulse repetition rate during ion implantation, because temperature of the workpiece during ion implantation process is influenced by the pulse repetition rate and the assumption is that the higher the frequency the higher the temperature of the workpiece and the more the ions penetrate deeper into the workpiece. The frequency or pulse repetition rate will be varied from 500 Hz to 250 Hz for sample P_2, and P_3 keeping pulse widths to 5μs. See the figure 1 below:

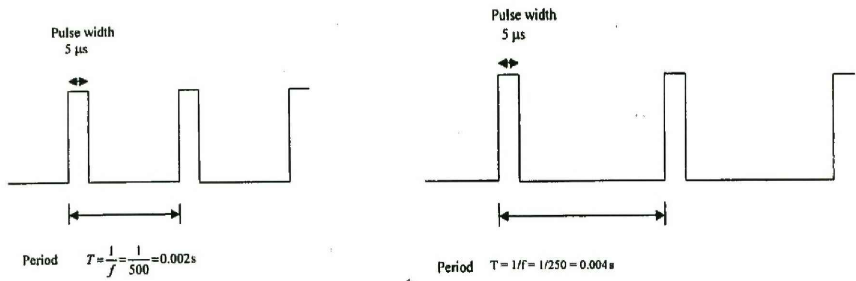

Figure 1.1: Shows schematic representation of pulses with frequencies 500 Hz and 250 Hz and also the pulse width of 5 µs.

1.2 Thesis Structure

This thesis is organized in this manner: Chapter 1 contains general introduction of the study, and chapter 2 outlines surface modification techniques while chapter 3 contains details of experimental equipment and techniques chapter 4 constitutes data analysis and results and chapter 5 is comprised of summary and conclusion.

Chapter 2

Surface Modification Techniques

Introduction

Surface modification is defined as a process whereby the surface properties of material are modified independently of the bulk properties [Mey01]. Often there is a need to harden the surface of the material, for example, drill bits with a hard surface that will provide better cutting edges and wear resistance. Although there are other forms of surface modification such as surface coating, surface hardening, gas nitriding, thermal annealing etc, particular attention will be given to Plasma source ion implantation as one of the surface modification techniques. Before PSII is discussed in detail a quick summary of other techniques is provided.

2.1 Surface coating techniques

There are many surface coating technique available [WWW1] which were developed years ago yet they are still in use and further modified. Those techniques range from nickel and zinc coatings for iron and steel with an intention of improving corrosion resistance and wear to the material. Coatings can be deposited in different forms, by physical vapour deposition (PVD) and chemical vapour deposition (CVD).

2.1.1 Physical Vapour Deposition (PVD)

PVD basically involves atom-by-atom, molecule-by-molecule, or ion deposition of various materials on solid substrates in vacuum systems; PVD uses atomic clouds formed by evaporation of the coating material in a vacuum environment to coat the surface. This PVD process can coat a thick 1 mm layer of heat resistant materials such as chromium, aluminiun and yittrium on jet engine parts. This process is associated with the following disadvantages [WWW3]:

- low to medium adhesion
- non-uniform thickness
- low penetration in deep holes and recesses.
- "line of sight" process.

Table below depicts the advantages and the disadvantages of surface coatings.

Table 2.1: Comparison of advantages and the disadvantages for surface coating.

Advantages	*Disadvantages*
- *Conducting and insulating samples/ targets can be coated.* - *A complex coating is possible.*	- *Layer delamination, extremely surface dependent.* - *Bonding failure and slight in increase dimensions.*

2.1.2 Chemical Vapour Deposition (CVD)

CVD is capable of producing thick dense, ductile layers with good adhesion on metals and non-metals. The process requires a metal compound that will volatilize at a fairly low temperature and decompose to a metal when it comes into contact with the substrate at high temperature. CVD is characterized by the following disadvantages:

- High deposition temperature of approximately 1000 °C
- Loss of hardness in the part being treated
- Significant dimensional changes and geometrical distortions.

2.2 Surface modification

2.2.1 Heat treatment

It's a combination of operations involving heating and cooling of a metal or alloy in the solid state for the purpose of obtaining certain desired properties. There are different forms of heat treatment, but two will be discussed briefly: Full annealing and stress relief annealing. Full annealing is defined as a process in which the steel is heated to a proper temperature and then cooled slowly through the transformation range. Basically the importance of this annealing process is to refine the grain, induce softness, improve electrical and magnetic properties and this process takes places in the furnace. Stress relief annealing or sub-critical annealing is useful in removing residual stresses due to cold-working processes (deforming metal plastically at a temperature lower than the recrystallization temperature). This process is associated with temperatures below the lower critical line (535-649) °C [Avn74].

2.2.2 Gas nitriding

It is linked to the history of ammonia. Here is a brief background of ammonia. In 1774 ammonia was presented in its free chemical form by Priestly, and a decade later as an elemental bond of nitrogen and hydrogen by a French chemist Claude-Louis Berthollet. In 1913 Haber and Bosch manufactured ammonia out of nitrogen and hydrogen, this led to industrial use of ammonia and it was found to have a good interaction with steel, then ammonia was utilized in the process called gas nitriding. This process involved the material of interest being subjected to heat of about 500 ^{0}C to 570 ^{0}C for 40 to 90 hours in an ammonia gas environment and desirable pressure, and that allows nitrogen to diffuse into the surface of the material.

2.3 Ion Implantation

Ion implantation is a process by which ions are accelerated to a target at energies high enough to bury them below the target's surface. There are several types of ion implantation, e.g. conventional ion implantation and plasma source ion implantation. Conventional ion implantation is a line-of-sight process because ions are extracted from an ion source, accelerated and focused into a beam, which is then rastered onto the target. Often the ion beam must be partially masked to prevent ions from striking the target at angles greater than 30° (degree) off-normal to ensure that most of the ions are implanted and reduce sputtering. The target must also be rotated and manipulated to insure that all parts are treated, see Figure 2.1. Plasma source ion implantation (PSII) is a non-line-of-sight surface modification technique. It is basically a technique by which the target is immersed in a plasma containing ions to be implanted. High voltage pulses are applied (10-150 kV) [Mat94], so during the voltage biasing process a sheath develops around the target, and then plasma ions in the vicinity of the target are accelerated by an electric field into the target and implanted. PSII has the following advantages as compared to conventional ion implantation.

- Elimination of beam rastering and target manipulation hardware.
- Elimination of target masking and reduction of surface sputtering and retained dose problems. The ion source hardware and control are at near ground potential.
- Greater production throughput, especially for large and diverse targets.
- The smaller, less expensive, easier to operate PSII hardware for "in house" operation, versus the "outside service facility" operation mode prevalent in the ion-beam industry [Mey01].

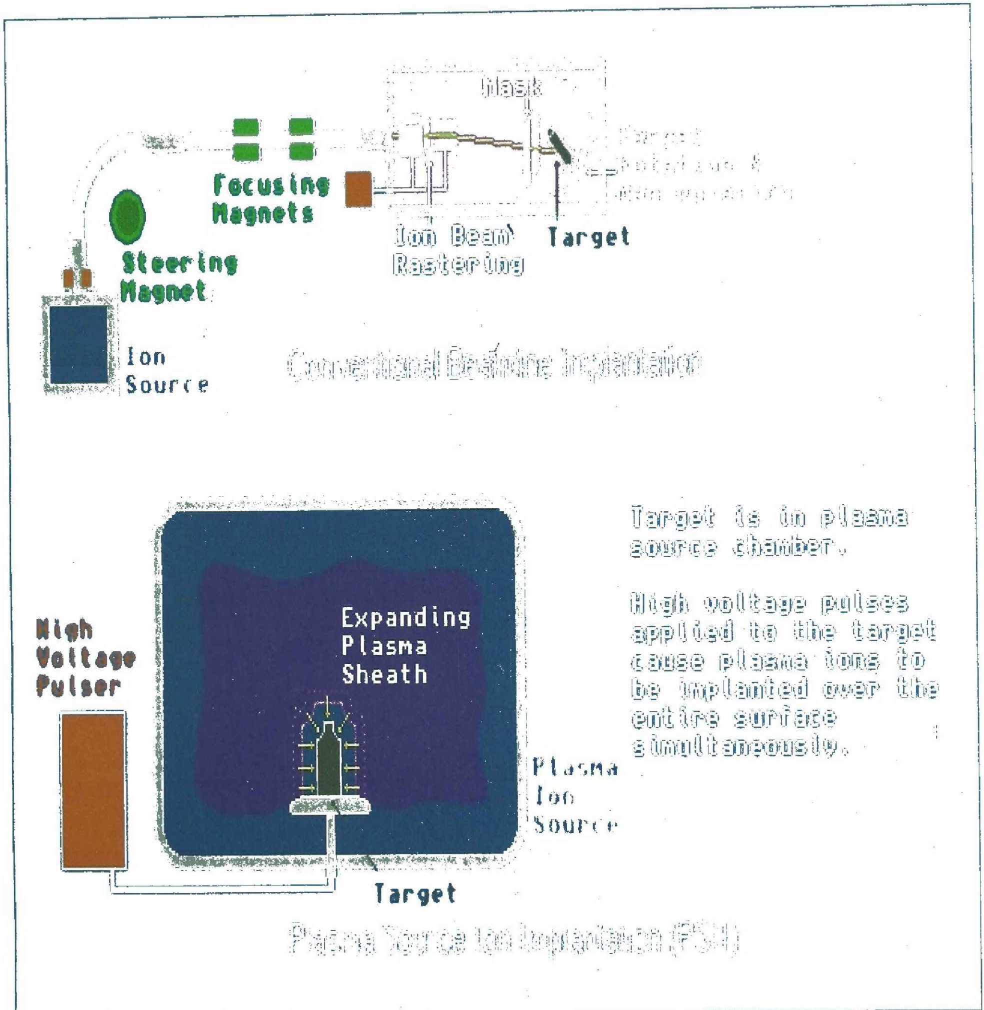

Figure 2.1: A comparison of the hardware requirements of conventional beam-line ion implantation versus PSII [WWW2].

2.4 Ion implantation process

Under ideal conditions, the time taken to implant the desired dose D, is given by the following equation [Mey01]:

$$t = \frac{D \cdot Q}{I_i \cdot A_S} \cdot \frac{Z}{M} \tag{2-1}$$

Where t is the implantation time, Q charge state of implantation ion species, I_i is the implantation current, A_S the implantation surface area and M/Z is the number of ions implanted per molecule. Real ion implantation processes are more complex because it includes effects such as sputtering, secondary electron emission and retained dose. Sputtering affect ion implantation by removing existing implanted ions and sets the limit of the maximum concentration of ions that can be implanted and retained in a workpiece, while secondary electron emission reduce ion implantation efficiency.

2.4.1 Sputtering

Sputtering is the erosion of a sample by energetic particle bombardment. In this study 20 keV nitrogen ions are implanted and will lead to sputtering effects. Sputtering can be characterized primarily by the sputtering yield, Y that is defined by [Nas96] as:

$$Y \equiv Sputtering\ yield = \frac{mean\ number\ of\ emitted\ atoms}{incident\ particle} \tag{2-2}$$

Sputtering processes occur when atoms are ejected from the outer surface layers because incident ions transfer energy to target atoms during collision. Then target atoms recoil with sufficient energy to generate other recoils. Some of these backward recoils will approach the surface with enough energy to escape from the solid. It is this secondary recoil, which makes up most of the sputtering yield (see Figure 2.3) [Nas96]. More complete of this theory is explained in the appendix A.

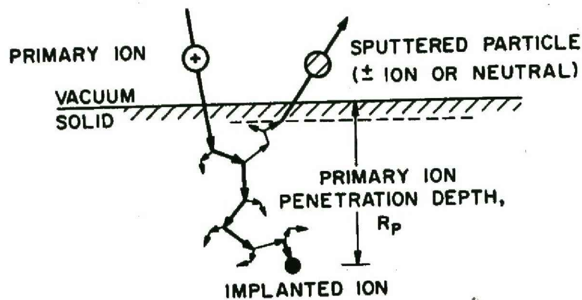

Figure 2.3: Schematic of ion-solid interactions and the sputtering process [May86]

Sputtering contributes to the compositional changes of the material but in our case, sputtering is minimized, because with PSII ions are implantated mostly perpendicular to the surface.

2.4.2 Secondary electron emission

Secondary electrons are produced when the high-energy ions strike the workpiece/target surface hence some of the energy from the high-energy ions cause emission of electrons from the workpiece. For example, a 20-keV N^+ ion incident on stainless steel has an electron emission coefficient of γ_{SE}= 4.8 which is the number of electrons emitted per incident ion [Fun00]. The electron emission coefficient can be seen in Table 2.2, which was determined by M.M Shamim *et al.* for different incident ion energies and for different materials [Sha91].

Table 2.2: Experimentally determined electron emission coefficient for nitrogen ions [Sha91].

	Energy (keV)		
Material	*20*	*30*	*40*
Stainless steel 304	*4.8*	*6.3*	*7.3*
Copper	*3.9*	*4.9*	*6.1*
Ti-6Al-4V	*5*	*6.2*	*7.7*
Graphite	*8.6*	*10.8*	...
Aluminum (oxidized)	*14.5*	*18.5*	...
Aluminum (etched)	*15.8*	*16.9*	*19.1*

This actually indicates that secondary electron emission is a factor that should not be ignored in ion implantation process, because when secondary electrons hit the wall of the plasma chamber, x-rays are produced and a significant amount of x-rays of energies between 9 and 11 keV are produced. Thus some of x-rays escape through the aluminium chamber wall into the room, however radiation protection measures should be taken when working at the plasma ion implantation facility [deV99]. Secondary electron play a role when implanted dose is evaluated, because it is assumed that whenever an ion is implanted there's a release of secondary electrons γ and then the ion current is $1/(1+\gamma)$ of the mean current.

2.4.3 Retained Dose

Ion implantation is limited by the retained dose even with sophisticated target manipulation systems however this gives space for plasma source ion implantation because of its advantages (no target manipulation, beam rastering and the retained dose problems are eliminated) over beam-line ion implantation. Retained dose by definition is a portion of the implanted ions that remain in the sample during ion implantation process. Retained dose is affected by the angle of incidence and the solubility of the implanted ion species in the workpiece while incidence angle accounts for both the probability of an ion penetrating into the sample and for the ion to remove one or more target ions (Sputtering). J.R Conrad *et al.* [Con89] demonstrated that the retained dose depends on the angle θ from the surface normal with which an incident ion strikes the workpiece and is approximated by:

$$R \propto \cos^{8/3}(\theta) \quad (2\text{-}3)$$

Where R is a retained dose and θ is an angle of incidence of ions. Retained dose has its maximum value at $\theta = 0^{\circ}$ as seen below on Figure 2.4 and preferred angle was less than 30^{0}.

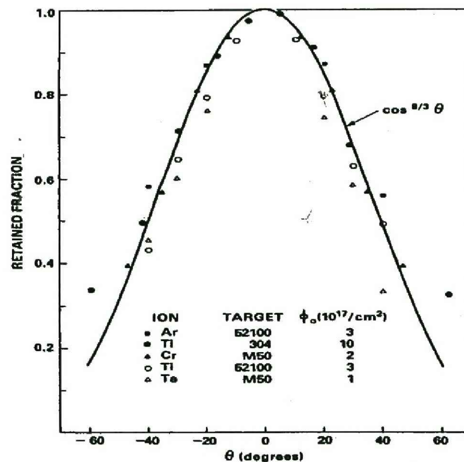

Figure 2.4: Shows the retained dose fraction, as a function of implant angle and within the graph there's examples of ion, target model and also the dose values. Taken from [Wit 85]

2.4.4 Plasma Formation

Plasmas produced by PSII are produced by electron bombardment of a neutral gas in an evacuated vessel. In the direct current discharge a current is past through a set of tantalum filaments to heat them by joule heating. A significant number of electrons are emitted in the hot filament, because their energy is greater than the work function and these electrons are called primary electrons. These primary electrons collide with neutral gas atoms such as hydrogen, argon or nitrogen with sufficient energy to remove valence electrons. The removed valence electrons are called secondary electrons, and their scattered with less energy than the incident primary electrons.

This method is a Glow Discharge and our focus is on this method even though there are other plasma forming methods such as electrodeless RF discharges (PIII); laser beams etc.

2.4.5 Ionization cross-section and mean-free-path

The mean-free-path (λ_m) is the mean distance between collisions defined in terms of momentum loss in collisions between electrons and neutral atoms. Mean-free-path is important because it is of assistance on defining the regime in which plasma is considered collision-less, hence simplifying the theory used to predict the process behavior. The probability of momentum loss can be expressed in terms of the equivalent cross-section σ that the atoms would possess if they were perfect absorbers of electron momentum, so the momentum transferred from the incident primary electrons gives the neutral gas atom enough energy and thus excites the atom to at least its first excited state, releasing secondary electrons, and the event is called an ionization event. Consider an electron incident upon a slab of area A and thickness dx containing n_n neutral atoms per unit volume, where each atom is an opaque sphere of cross-section area σ and the number of atoms in slab as show on Figure 2.5 is:

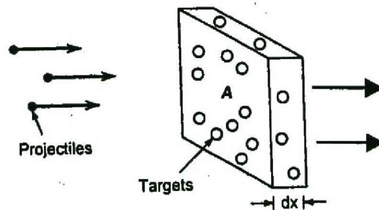

Figure2.5: Illustration of the definition of cross section

$$n_n \, A \, dx \qquad (2\text{-}4)$$

The fractional of the slab block by atoms is:

$$\frac{n_n A dx \sigma}{A} = n_n \sigma \, dx \qquad (25)$$

If a flux Γ of electrons is incident on the slab, the flux emerging on the other side is

$$\Gamma' = \Gamma\left(1 - n_n \sigma \, dx\right) \qquad (2\text{-}6)$$

Thus the change of Γ with distance is:

$$\frac{d\Gamma}{dx} = -n_n \sigma \Gamma \qquad (2\text{-}7)$$

Or

$$\Gamma = \Gamma_0 e^{-n\sigma x} \equiv \Gamma_0 e^{-x/\lambda_m} \qquad (2\text{-}8)$$

Therefore in a distance λ_m the flux would decrease to 1/e of its initial value. Hence quantity λ_m is the mean-free-path for collision:

$$\lambda_m = \frac{1}{n_n \sigma} \qquad (2\text{-}9)$$

2.4.6 Primary electron current limitations

There are two factors that limit primary electron current:

- Space charge
- Cathode temperature

2.4.6.1 Space Charge Limited Emission

The space charge limited current is given by the Child- Langmuir Law [Lan23]

$$J_{SC} = \frac{4}{9}\varepsilon_0 \left(\frac{2e}{m_e}\right)^{1/2} \frac{u^{3/2}}{d^2} = 2.33 \times 10^{-6} \frac{V_d^{\ 3/2}}{d^2} \qquad (2\text{-}10)$$

Where V_d is the discharge bias in volts, d the distance between the anode and the cathode in cm and J_{SC} is expressed in units of $A.cm^{-2}$, if the discharge voltage is V_d = 60 V and d = 5 cm J_{SC} becomes ≅ 40 $\mu A.cm^{-2}$ for our system.

2.4.6.2 Temperature Limited Emission

The temperature limited emission current is given by Richardson Law:

$$J_T = BT^2 e^{-w/kT} A.cm^{-2} \qquad (2\text{-}11)$$

Where W and T are work function and temperature of the filament metal, $B = 4\pi m_e k^2 / h^2 = 120 A.cm^{-2}.K^{-2}$. Since the Tantalum (Ta) filament is used as a filament metal during production of plasma, Ta filaments has a work function w=4.25$eV.K^{-1}$ and the melting point is 3269 K. The Richardson law gives for Tantalum at 2000 K, $J_T \approx 9\, mA.cm^{-2}$.

2.4.7 Temperature versus space charge limitations

$J_{SC} << J_T$, so the discharge current, which is just the emission current, is a sensitive function of the filament temperature and surface area. Since plasma density is proportional to discharge current, there is a need to monitor the discharge current and control the filament temperature, thus maintain a constant discharge current independent of fluctuations in filament temperature, as the bombarding ions sputter away the filament.

2.4.8 Plasma Sheath Theory

A Plasma sheath is a region in which charge imbalances exist in the vicinity of solid or liquid boundary [Mah94]. Sheaths are found for example, on plasma confining walls, on electrodes and around probes immersed in plasma. The basic plasma sheath physics is noted in this fashion, since the electron thermal velocity $(eT_e / m)^{1/2}$ is at least 100 times the ion thermal velocity $(eT_i / M)^{1/2}$ because m/M<< 1 and $T_e \geq T_i$, where T_e and T_i given in units of volts. Therefore consider a plasma of width l with $n_e = n_i$ initially confined between two grounded $(\Phi = 0)$ absorbing walls see figure 2.6a. Since the net charge density denoted by $\rho = e(n_i - n_e)$ is zero, the electric potential Φ and the electric field E_x is zero everywhere [Fun00]. Hence (a) is transformed to (b) as shown in Figure 2.6 due to the fast moving electrons that are not confined and are lost near the walls. When $n_i >> n_e$, thin positive ion sheaths form near each wall, thus net positive ρ within the sheaths leads to a potential profile Φ(x) that is positive within the plasma and falls to zero near both walls and this acts as a confining potential for electrons and ions, therefore since electric fields within the sheath points from the plasma to the walls, then force $F = -eE_x$ acting on the electrons is directed into the plasma and this reflects the electrons moving towards the walls back into the plasma. On the other hand ions from the plasma that enter the sheaths are accelerated into the walls.

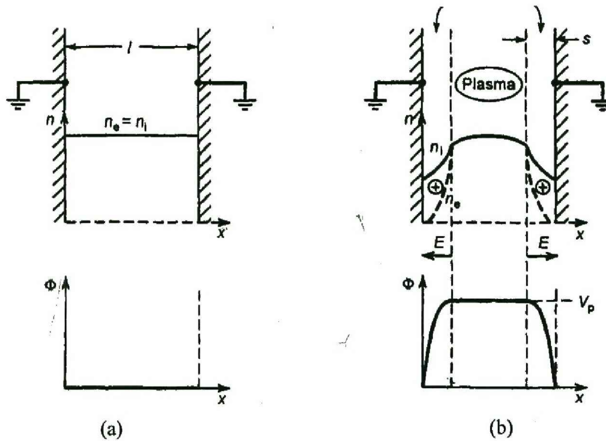

Figure 2.6: Formation of plasma sheath: (a) Initial electron and ion densities and potential (b) densities, electric field and potential after formation of the sheath.

When a pulse of amplitude $-V_0$ is applied to the workpiece at $t = 0$, then as time evolves on the time scale of the electron plasma period $\left(w^{-1}{}_{pe}\right)$ electrons near the surface are driven away leaving behind uniform density ion matrix sheath. On the time scale of the ion plasma period $\left(w^{-1}{}_{pi}\right)$, ions within the sheath are accelerated into the workpiece leaving a nonuniform, time varying ion density near the workpiece. This behaviour during the pulsing process is shown below on figure 2.7:

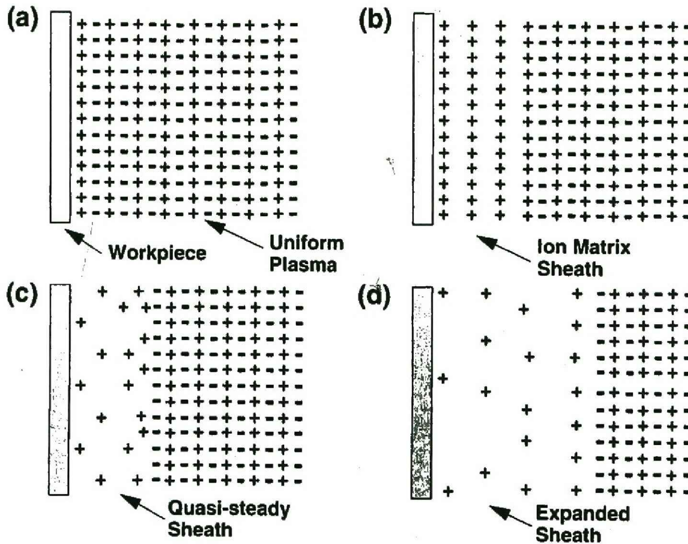

Figure 2.7: Time evolution of the plasma sheath during the PSII pulse: (a) $t = 0$, initial conditions; (b) t at ≈ 5 ns repulsion of electrons near the surface of the workpiece to form the ion matrix; (c) at $t \approx 1 \mu s$, quasi-steady, space charge limited ion flow across sheath, (d) at $t \approx 10$ μs, space charge limited flow in the expanding sheath [Nas96].

- Figure 2.7(a) In a short time after voltage application, typically some several nanoseconds, plasma electrons are driven away from a layer near the surface of the target. This electron motion is a displacement current that charges a plasma capacitance.
- Figure 2.7(b) At this stage plasma sheath comprises of motionless ions, due to their larger inertia, and this uniform ion layer is called ion matrix sheath.
- Figure 2.7(c) At this phase quasi-steady ion current flow is achieved with space charge limited current density across the sheath governed by Child-

Langmuir Law. As ions are implanted, charge imbalance drives electrons away from the target, forcing the sheath to expand outward from the target to reveal more ions.

- Figure 2.7(d) At this stage the pulse length and plasma ion density are adjusted for the sheath to remain contained in the vessel.

NWU LIBRARY

CHAPTER 3

Experimental Equipment and Analytical Techniques Background

3.1 Plan View

The study is based on implanting materials with nitrogen using the plasma source ion implantation (PSII) laboratory, which is a cable intensive laboratory situated on the first floor of the Materials Research Group building. The PSII machine was designed and constructed for use to broaden the scope of research of the group [Mey01]. Figure 3.1 shows the location of the laboratory:

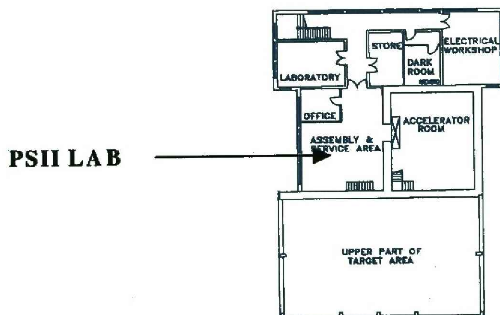

Figure 3.1: PSII Lab situated in the assembly and service area.

The laboratory is next door to the upper region of the vertical electrostatic Van de Graaff accelerator. In front of the machine itself or more specifically beside the pulse generator, a wall was erected to act as a barrier for x-rays produced by the pulse generator during its operation. The pulse generator is capable of producing x-rays, especially at high negative voltages (≥18 kV), so it was necessary to build a concrete block wall beside the machine for safety purposes.

3.2 PSII Features

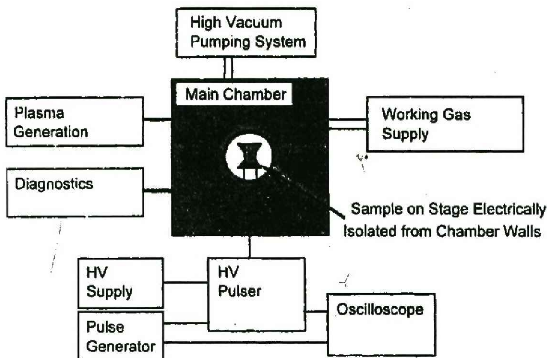

Figure 3.2: Typical example of schematic diagram for the PSII system [Fun00]

3.2.1 Main Chamber

The facility consists of two main components, plasma chamber and RUP-4a (Rossendorfer Universal Pulsgenerator- economy version) high voltage pulsed power supply. The plasma chamber is an aluminium alloy chamber in the form of the joining of two cylinders, the main cylinder has a radius of 0.33 m and is 1.04 m in length while the smaller cylinder of the union houses the filament assemblies, each side protrudes from the plasma chamber by 0.23 m with ~ 0.24 m inner radius. The chamber has flanges on all sides. The rear flange was designed to accommodate the high voltage feedthrough from the high voltage pulsed power supply. The front flange contains view ports, probe hardware that includes 6 stepper motors for 2 motorized probes and a third manually operated probe. The bottom flange accommodates the diffusion vacuum pump, which the top flange was designed to accept the high-voltage feedthroughs required for the 13.65 MHz Radio Frequency (RF)- antenna, while the

side flanges where designed to cater for numerous smaller electrical feedthroughs, each side consists of two small view ports which are manufactured out of armour glass. Figure 3.3 shows the schematic diagram for plasma chamber.

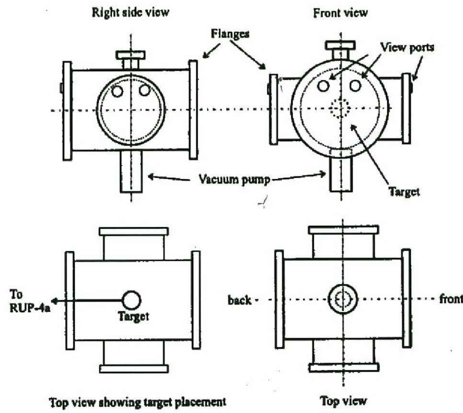

Figure 3.3: Schematic diagram depicting the plasma aluminum alloy chamber [Mey01].

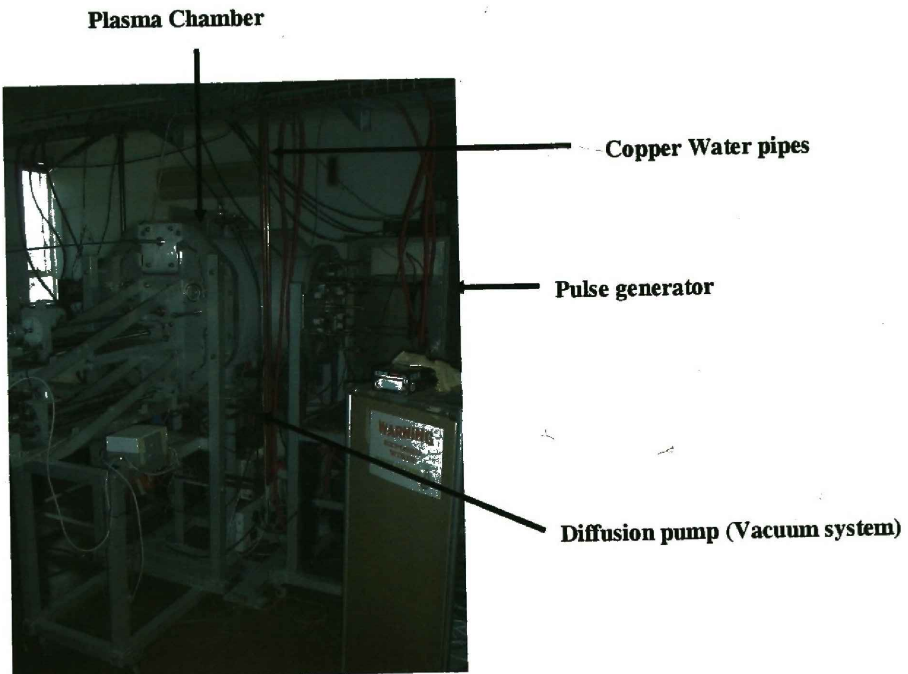

Figure 3.4: Photograph of the PSII chamber and also RUP-4a pulse generator beside the chamber.

3.2.2 Vacuum pumping system

Oil diffusion pump and turbo molecular pump was used to pump vacuum chamber down to pressures in the high vacuum range. Since cooling is essential both oil diffusion pump and turbo molecular pump, a water-cooling circuit was already installed in the facility to cool the vacuum pumps and the steel conductors delivering electricity to the tantalum filaments. Copper pipes were constructed to carry water from the ground floor, see Figure 3.4. Water rate sensor was included in the system to ensure a minimum water flow rate in the cooling system. Two filters (*60 μm* coarse sieve and *1 μm* fine filter) for removing physical impurities and to minimize potential sources of blockage and build-up in the *4mm* diameter chamber cooling waterways also form part of the system.

3.2.3 Plasma generation

Inside the plasma chamber there are two stainless steel electrodes, used for current delivery from the filament power supply, to the thin tantalum filaments wires *(0.1 mm diameter)*. These stainless steel electrodes are 15 cm apart and attached to a grounded backing plate. Thin tantalum filaments wires, which were wound to 6 mm diameter stainless steel electrodes, were used to produce primary electrons for ionization process.

3.2.4 Working Gas supply

Nitrogen gas is supplied by a high-pressure cylinder, which is connected to the chamber by a tube. There are regulators mounted on the gas cylinder. These regulators are used to regulate nitrogen gas flow from the gas cylinder to the plasma chamber. One of these regulators is below the needle Valve on the plasma chamber.

The needle valve is used to regulate the chamber pressure to suitable low chamber pressure values *(7-8 x10^{-4} mbar).*

3.2.5 Pulse generator

The pulse generator is an essential component of PSII. The generator used was designated RUP-4a (Rossendorfer Universal Pulsgenerator-economy version), it has implantation power supply capability for small to medium plasma ion implantation applications. The unit is controlled either through an internal pulse generator and voltage control or via an external pulse generator and *(0-10 V)* voltage source [Mey01]. RUP-4a is assembled in a 1.6-metre tall cabinet; the internal structure of the cabinet is separated into four distinguishable compartments as depicted below in Figure 3.5:

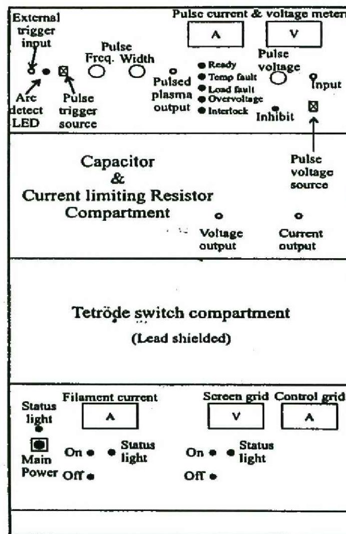

Figure 3.5: Layout of the RUP-4a power supply cabinet.

At the bottom there is switching control electronics and main power transformer, the bottom front panel houses the main power switch, the push-button switches to enable

and disable the tube grid and filament power supplies and the analogue meters used to monitor the filament current, screen grid voltage and control grid voltage. The bottom rear panel houses the connectors for mains input, the interlock and the grounding lug. The middle bottom section contains the EIMAC 8960 tetrode thermionic Valve. Since x-ray radiation are given off due to bremsstrahlung emission the compartment must be lead shielded and not be opened when the machine is in operation. The middle top compartment houses the current limiting resistors and the storage capacitor. It also houses the current monitoring circuits, with the appropriate BNC connectors on the front panel, and the antenna used for arc detection. The high-voltage co-axial cable emerges from the side panel compartment. The top compartment houses the DC HV capacitor charging module, the internal pulse generator circuits and the arc detection circuit. The front contains the variable resistors for the pulse timing and voltage control, switches and connectors to select external control and the analogue meter displaying the currently output implantation potential.

3.2.6 Diagnostics

Langmuir Probes are used as diagnostics tools, to determine the state of plasma parameters, for example the electron density (n_e) and the electron temperature, the floating potential (ϕ_f) and also the plasma potential (ϕ_p). The front flange of the plasma chamber has two stepper motor controlled probes coupled with hardware and software assembled to operate one these probes. The function of the two stepper motors is to position the probe anywhere on the two dimensional plane in the cylindrical co-ordinates determined by z and θ for a fixed r, with respect to the length of the short arm of the probe. The geometry of these probes is as seen below on Figure 3.6.

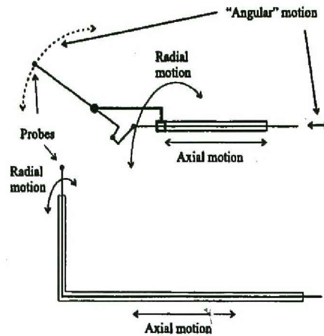

Figure 3.6: Diagram depicts the layout and basic operation of the two Langmuir probes. The lower probe is a fixed L- shaped arm, which basically restrict the position of the probe to the surface of the cylinder. The upper probe has pivots which enable them to be positioned anywhere within the volume of a cylinder [Mey01].

3.2.7 Oscilloscope

It was used for monitoring the implantation voltage and current. The oscilloscope is connected to the two BNC connectors (short for British Naval Connector or Bayonet Nut Connector [WWW4]) on the front panel of the pulse generator, these BNC connectors produce *1:5000* and *1:10* representative signal of voltage and the implant current as outputs to the oscilloscope.

3.3 Stopping and Ranges of Ions in Matter

SRIM is a group of programs, which calculate the stopping, and range of ions *(10 eV-2 GeV/amu)* into matter [SRIM00]. SRIM is abbreviated from **S**topping and **R**anges of **I**ons in **M**atter. SRIM has several versions like TRIM-91, 95 and 2000.This program is used to calculate the stopping and the range of ions of particular energy and also capable of calculating both the final three dimensional distribution of the ions and all kinetic phenomena associated with the ion's energy loss, target damage, sputtering, ionization and phonon production. Example for SRIM calculations is

shown on Figure 3.7 for ion ranges and sputtering. Nitrogen ion of energies *20 keV* was selected and the target material such as typical stainless steel of density *8.0 g/cm*^{3} and composition Cr-*8%*, Fe-*74%* and Ni-*18%* with layer (*1000 angstroms*) of interest was defined and the program was executed to calculate the ion range and sputtering. The nitrogen ion distribution range into stainless steel was given as *243* angstroms after running the program at this default number of ions (*99999*) for TRIM calculations. The program can be downloaded from the following website: http://www.srim.org/.

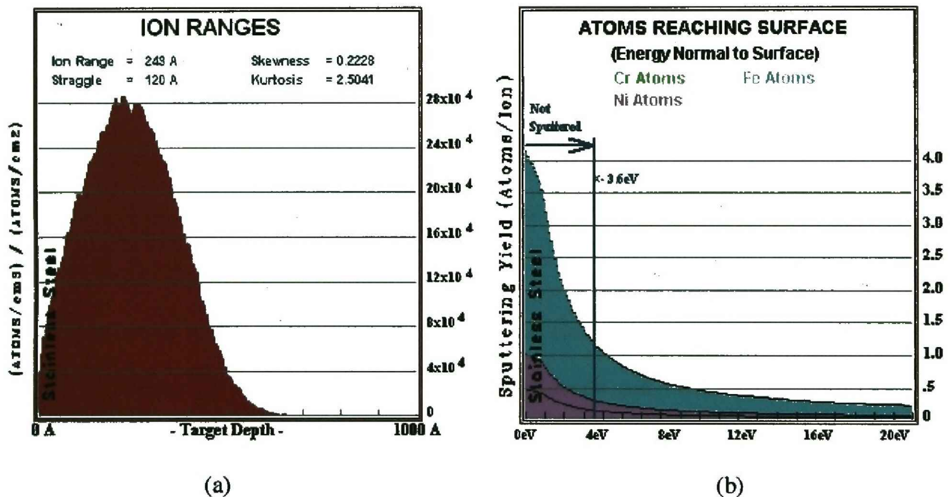

Figure 3.7: (a) Show the ion ranges (243 A) for nitrogen ions as incident ions at 20 keV into stainless steel; straggle; skewness and kurtosis and (b) depict sputtered atom yield vs. energy.

3.4 Sample preparation

Slab shaped mild steel (*0.25 %*C.AISI NO: C*1025*) [Avn74] targets were polished to a mirror finish to get rid of coarse irregularities that tend to affect analysis. The standard method of preparing samples for implantation was followed. Grinding under flowing water with sand paper of decreasing roughness from *200* down to *600* roughness was performed to remove coarse irregularities. All scratches coarser than the current grinding were removed. The final grinding was done by using water paper (*1000* roughness), followed by thoroughly cleaning samples in ultrasound alcohol bath, to get rid of coarse contaminants left behind by the sand paper. The first polishing stage was achieved by using $3\ \mu m$ diamond paste on a polishing disk followed by cleaning in alcohol and final polish with $0.25\ \mu m$ diamond paste. After diamond paste polishing stages the sample was examined under optical microscope to ensure that no scratches remain in the area of interest.

3.5 Target insertion

A pinhole was made into mild steel target, so as to clamp the target with a rod like steel sample holder for a better support between the target and a rod. Sample holder was covered with a glass tube to restrict implantation on a sample holder. The sample holder was inserted in the plasma chamber at the center of the rear flange were high voltage electrode is positioned. The center of the rear flange accommodate copper electrode, which is insulated by polytetrafluoroethene (PTFE) and connected to the HV coaxial cable. Approximately $1.26\ cm^2$ area of a sample holder was exposed to the plasma see figure 3.8 and the target area exposed to the plasma was $\approx 6\ cm^2$.

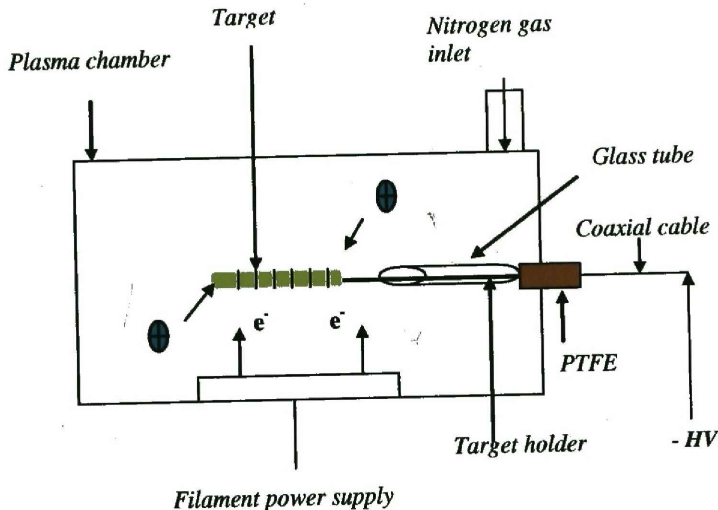

Figure 3.8: Diagram showing the setup of a target and target holder inside the plasma chamber.

3.6 NetLab Software

The NetLab Software basically describes a suite of programs written to facilitate operation of the PSII facility and enabling the operator to monitor chamber pressure, implantation voltage and current and also to control the RUP-4a power supply. The software can also perform complex calculations and present data with the powerful graphical abilities of interactive data language (IDL). NetLab software suite consists of two distinct components namely: The User interface and NetLab Kernel. The user interface is written in IDL and presents the user with a graphical user interface (GUI) and used to control most of the implantation parameters while NetLab kernel is written in "C" programming language and it runs in Linux, its purpose is to accept

commands from the user interface with data capture hardware. Netlab software was used to perform tasks mentioned above during ion implantation. See diagrams below depicting experiment application window and implantation control window [Mey01].

3.6.1 Experimental application window

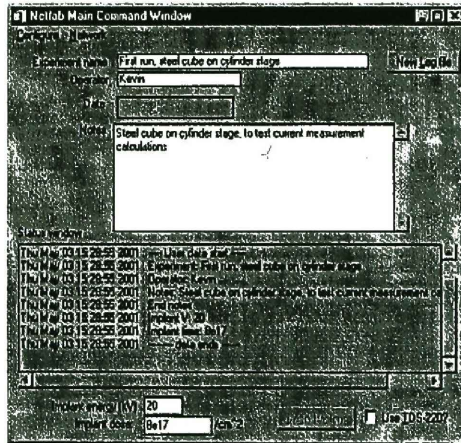

Figure 3.9: Typical example of netlab software window, which experiment details can be defined [Mey01].

The experiment application window allows the operator to configure the software and connect to the Netlab Kernel and also describe the details of the experiment. The window also allow the user to select the log file for capturing experiment events and has a space for notes about the experiment and there is also a button used to invoke optional Tektronix TDS-220 oscilloscope window to show current and voltage pulse.

3.6.2 Implantation control window

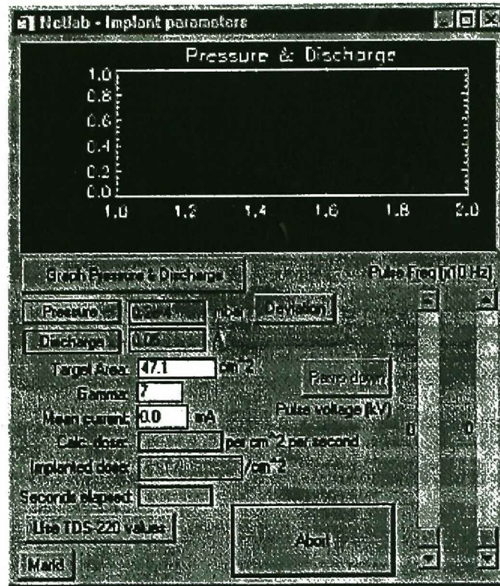

Figure 3.10: Example of Implantation window depicting defined implantation parameters [Mey01].

This window, allows the operator to define the target and implantation parameters. Thus if TDS-220 is connected, the mean current can be determined automatically. Large ABORT button is used to shut down the RUP-4a. Implanted dose calculations are given by:

$$D\left(ions/cm^2\right) = \frac{\text{Implanted Charge}}{\text{Target area}} = \frac{I_{mean}/(1+\gamma)}{\text{Target area}} \quad (3\text{-}1)$$

Where I_{mean} is the mean current and γ is the secondary emission coefficient.

3.7 Analytical Techniques

The facilities at the Material Research Group (MRG) primarily employ nuclear and x-ray technologies such as nuclear reaction analysis (NRA), Rutherford Backscattering Spectrometry (RBS), Particle induced x-ray emission (PIXE), Elastic Recoil Detection Analysis (ERDA) and X-ray diffraction. The technique of interest was NRA, because of its capability for profiling elements of low-Z in the presences of heavier elements in the matrix. RBS was also employed.

3.8 General Theory

The principles for these nuclear techniques are similar and are explained in this way: an incident particles penetrates the target where it interacts with a target atoms to produce a reaction particle in a binary collision. In RBS a beam of mono-energetic He^+ ions or known particles with mass M_1 is accelerated (given energy E_0) and directed to a target containing target atoms of mass M_2, see figure 3.11. A small fraction of impinging ions will backscatter at angle greater than 90^0. The energy E_1 and the angle θ of particle M_1 are detected. From conservation laws of energy and momentum, mass of the target atoms M_2 is deduced and the abundance of M_2 can be estimated by counting the yield of the scattered particles of mass M_1, captured by a detector at a certain solid angle. Elastic Recoil Detection analysis is similar to RBS but instead of recording the scattered incident particle the lighter recoiling nucleus is measured directly in forward direction. If E_1 and M_1 are the incident energy and mass and E_2 recoiling energy with mass M_2 then [Pre88]

$$E_2 = k\,E_1 \tag{3-2}$$

Where k is a kinematic factor given by:

$$k = \frac{4M_1 M_2}{(M_1 + M_2)^2} \cos^2 \phi \qquad (3\text{-}3)$$

ϕ is the hydrogen recoil angle. NRA is based on nuclear reaction between incident particle and the target nuclei. One important point is that if the interaction does not occur at the target surface both the incident and outgoing particles or ions lose energy as they traverse the material. The energy loss is due to the stopping power of the target matrix. The projectile interaction is determined by the following two phenomena: Cross-section, which is the probability that the reaction will occur and the kinematic factor which determines the energy of emerging or outgoing particles.

3.8.1 Kinematic Factor

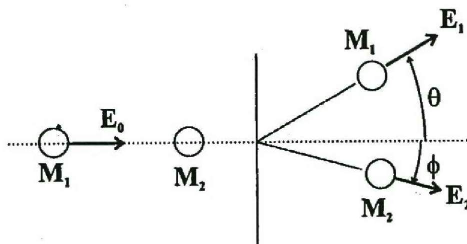

Figure 3.11: A schematic representation of a collision in the laboratory frame of reference.

The kinematic factor is the ratio of projectile energy immediately after scattering to incident energy and immediately before scattering. See figure 3.11. An incoming projectile with mass M_1 and energy E_0 strikes a target atom with mass M_2 at rest. For RBS the resultant scattered particle has energy E_1 at an angle θ with respect to the incoming beam and for Elastic recoil detection analysis (ERDA) the target atom recoils at an angle ϕ and energy E_2. The kinematic factor for RBS is given by:

$$K = \frac{E_{scattered}}{E_{incident}} \left[\frac{\left\{1 - \left(\frac{M_1 \sin\theta}{M_2}\right)^2\right\}^{1/2} + \frac{M_1 \cos\theta}{M_2}}{1 + \frac{M_1}{M_2}} \right]^2 \quad (3\text{-}4)$$

3.8.2 Stopping Power

Few stopping models have been developed but the most common are the Andersen-Ziegler [And77] and the Ziegler-Biersack [Zie85] theories. Stopping power is explained in this way, when the projectile penetrates into the target matrix, it loses energy due to collisions with the electron shell and target nuclear. At low ion energies the nuclear energy loss is dominating, while at high ion energies the electronic stopping finally dominates. The energy loss per depth or stopping power determines the energy dE loss by a projectile traversing a segment of target thickness dx and is given by:

$$\frac{dE}{dx} = \left.\frac{dE}{dx}\right|_n + \left.\frac{dE}{dx}\right|_e \quad (3\text{-}5)$$

Or

$$dE/dx\left(eV/10^{15}\ atoms/cm^2\right) = S_e(eV) + S_n(eV) \quad (3\text{-}6)$$

Where S_e and S_n are electronic stopping and nuclear stopping power respectively.

3.8.3 Stopping in compounds

Bragg's rule [Bra05] is applicable in the determination of the stopping power of compounds, basically Bragg's rule state that the stopping cross-section $\varepsilon^{A_m B_n}$ of composition A_mB_n is given by $\varepsilon^{A_m B_n} = m\varepsilon^A + n\varepsilon^B$ where ε^A and ε^B are the stopping cross-sections of the atomic constituents A and B and is a simple linear additivity rule of stopping contributions of different compound elements. For a compound consisting of different elements i with atomic concentrations c_i ($\sum_i c_i = 1$) the total stopping power is given by:

$$S = \sum c_i\, s_i \qquad (3\text{-}7)$$

Where S_i is the stopping power of each element. Bragg's rule assumes that the interaction between the ion and the atom is independent of the environment. From observations, the chemical and physical state of the medium has an effect on energy loss. Deviations from Bragg's rule predictions are pronounced for solid compound such as oxides, hydrocarbons and nitrides by the order of *10-20 %.*

3.8.4 Evaluation of energy loss

The energy E of a particle in the depth x is given by the integral equation:

$$E(x) = E_o - \int_0^{x/\cos\theta} \frac{dE}{dx'} dx' \qquad (3\text{-}8)$$

Where E_o is the particle energy at the surface, θ is the angle between the ion beam and surface normal (See Figure 3.8) and $\frac{dE}{dx}$ is the energy dependent stopping power.

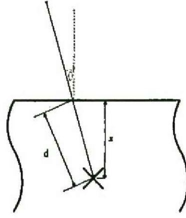

Figure 3.12: Depict the depth scale where the beam particle penetrates to a depth x, traversing a distance $d = x/\cos\theta$.

3.8.5 Cross-section

It is expressed in two regimes namely Rutherford regime and non-Rutherford regime, those regimes are discussed below.

3.8.6 Rutherford cross-section

Regimes with which Rutherford scattering cross-section can be determine are as follows: 1.The incident particle energy must be high enough that it can approach the target nucleus without being deflected by the target electrons. 2. To avoid nuclear force interactions, the projectile energy should not be too high such that the smallest distance between them approaches the dimensions of the nuclei. The Rutherford cross-section for backscattering is given by [Tes95].

$$\frac{d\sigma_{RBS}}{d\Omega} = \left(\frac{Z_1 Z_2 q_e^2}{4E}\right) \frac{4\left\{\left(M_2^2 - M_1^2 \sin^2\theta\right)^{1/2} + M_2\cos\theta\right\}^2}{M_2 \sin^4\theta \left(M_2^2 - M_1^2 \sin^2\theta\right)^{1/2}} \tag{3-9}$$

Where θ is the scattering angle, Z_1 and M_1 are the nuclear charge and mass of the incident particle, and Z_2 and M_2 are the nuclear charge and the mass of the target atom respectively. $\frac{d\sigma_{RBS}}{d\Omega}$ is the differential cross section in the laboratory system. Experimental measurements show that actual cross-section deviate from Rutherford at high and low energies for example carbon and oxygen ion scattering experiments on Al, Si and Ti were conducted. For carbon ion 6% deviations from Rutherford cross sections at laboratory kinetic energies of *15 MeV*, *15 MeV* and *22 MeV* for three respective targets were found [Boz93]. Low energy departures created by partial screening of nuclear charges is taken into account by a correction factor F:

$$\sigma = F\sigma_R \tag{3-10}$$

For $\theta > 90°$, correction factor (F) is given by L'Ecuyer et al [Lec79].

$$F_{L'Ecuyer} = 1 - \frac{0.049 Z_1 Z_2^{4/3}}{E_{cm}} \tag{3-11}$$

Where E_{cm} is the center of mass system (in keV). For $\theta < 90°$ correction factor is given by Andersen et al [And80].

$$F_{Anderson} = \frac{\left(1 + 1/2\frac{V_1}{E_{cm}}\right)^2}{\left\{1 + \frac{V_1}{E_{cm}} + \left[\frac{V_1}{2E_{cm}Sin\theta_{cm}/2}\right]^2\right\}^2} \tag{3-12}$$

Where θ_{cm} is the scattering angle in the center of mass system and the increase in the Kinetic energy, V_1 is given by:

$$V_1[keV] = 0.04873 Z_1 Z_2 \left(Z_1^{2/3} + Z_2^{2/3}\right)^{1/2} \tag{3-13}$$

3.8.7 Non-Rutherford cross-section

At high energies the cross-section deviate from Rutherford due to the influence of the nuclear force. Bozoian [Boz93] described a formula for E_{NR} for which deviation from Rutherford can be expected.

$$E_{NR}[MeV] = \left| \frac{M_1 + M_2}{Z_2} \frac{Z_2}{10} \right. \qquad for \ Z_1 = 1 \tag{3-14}$$

$$E_{NR}[MeV] = \left| \frac{M_1 + M_2}{M_2} \frac{Z_1 Z_2}{8} \right. \qquad for \ Z_1 > 1 \tag{3-15}$$

Where E_{NR} is the energy at which the non-Rutherford cross-section deviates by more than 4 %.

3.8.8 Nuclear reactions Kinetics

	Mass	*Energy*
Incident ion	M_1	E_1
Target nucleus	M_2	*0*
Light product	M_3	E_2
Heavy product	M_4	E_4

Table 3.1: Shows nuclear reaction quantities useful for the calculations of nuclear reactions kinematics.

The energy released in the reaction is Q (called Q values) when Q value is positive the nuclear reaction is exothermic reaction and when the Q value is negative the reaction is endothermic nuclear reaction and the Total energy is $E_T = E_1 + Q + E_3 + E_4$

By definition the following quantities:

$$A_{13} = \frac{M_1 M_2}{(M_1 + M_2)(M_3 + M_4)} \frac{E_1}{E_T}$$

$$A_{14} = \frac{M_1 M_4}{(M_1 + M_2)(M_3 + M_4)} \frac{E_1}{E_T}$$

$$A_{23} = \frac{M_2 M_3}{(M_1 + M_2)(M_3 + M_4)} \left(1 + \frac{M_1}{M_2} \cdot \frac{Q}{E_T}\right)$$

$$A_{24} = \frac{M_2 M_4}{(M_1 + M_2)(M_3 + M_4)} \left(1 + \frac{M_1}{M_2} \cdot \frac{Q}{E_T}\right) \tag{3-16}$$

Give the energy of the light particle created in the nuclear reaction by the following formula:

$$E_3 = E_T \, A_{13} \left[\cos\theta \pm \left(\frac{A_{24}}{A_{13}} \sin^2\theta \right)^{1/2} \right]^2 \tag{3-17}$$

Where θ is the particle emission angle. This equation has got two solution but the plus sign is only used when $A_{13} < A_{24}$ and the maximum possible emission angle is presented by:

$$\theta_{max} = \arcsin \left(\frac{A_{24}}{A_{13}} \right)^{1/2} \tag{3-18}$$

For the energy of the heavy particle with emission angle ϕ the equation is given by:

$$E_4 = E_T \, A_{14} \left[\cos\phi \pm \left(\frac{A_{23}}{A_{14}} - \sin^2\phi \right)^{1\backslash 2} \right]^2 \tag{3-19}$$

Thus only the plus sign is used for $A_{14} < A_{23}$ while for $A_{14} > A_{23}$ both solutions exist and the maximum emission angle is given by the following equation:

$$\phi_{max} = \arcsin \left(\frac{A_{23}}{A_{14}} \right)^{1/2} \tag{3-20}$$

3.8.9 Straggling

When energetic beam of charged particles penetrates the matter or the target the slowing down is accompanied by a spread in the beam energy and it is due to statistical fluctuations of the energy transfer in the collision process. Energy loss straggling has the following contributions: 1. Statistical fluctuations in the transfer of energy to electrons. 2. Statistical fluctuation in the nuclear energy loss. 3. Straggling due to multiple small angle scattering, resulting in angular energy spread on the ongoing and outgoing paths.

3.8.10 Nuclear Reaction Analysis

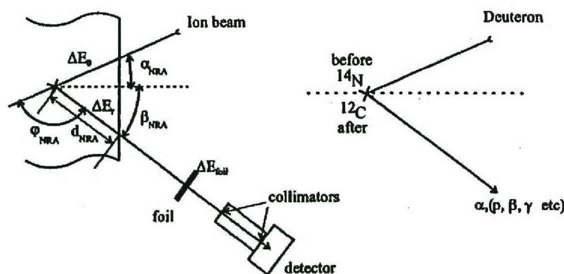

Figure 3.13: NRA experimental setup. On the right incident and the detected emission particle is shown and on the left the experiment angles α_{NRA}, β_{NRA} and φ_{NRA}, where α, β and φ are incident angle, exit and scattering angles respectively. Depths are also defined.

NRA is a non-destructive technique suitable on profiling light elements in the presence of heavier elements. It was used to determine nitrogen depth profiles in mild steel samples (*0.25%* C). NRA involves nuclear reaction between a target nucleus and incident particle. If the incident particle has sufficient energy to penetrate the coulomb barrier of the target nucleus, its energy is imparted to the nucleons and nuclear

reactions occurs. Reactions result in the emission of reaction product particles. Deuteron beam of about *1.2 MeV* was used, because is capable of inducing nuclear reactions such as $^{14}N(d,\alpha_0)^{12}C$, $^{14}N(d,\alpha_1)^{12}C$, $^{14}N(d,p_0)^{15}N$, $^{14}N(d,p_{1,2})^{15}N$, *and* $^{14}N(d,p_3)^{15}N$. For safety point of view the deuteron beam was kept as low as possible, because number of generated neutrons increases exponentially with deuteron energy. Setup above as indicated by the figure 3.13 shows a typical scattering geometry used in NRA experiments. α_{NRA} and β_{NRA} are the angles of incident beam and the detector relative to the surface normal of the target surface and φ_{NRA} is the scattering angle and in front of a detector there is absorber foil. A measured spectrum which is a function of energy and concentration for any single reaction can be determine as a function of depth from this equation:

$$E_r = E_3 - \Delta E_3 - \Delta E_{foil} \qquad (3\text{-}21)$$

Where ΔE_{foil} and ΔE_3 are energies lost by the emitted particle as it leaves the substrate and traverses the absorber foil (Mylar foil) and E_3 is given by equation (3-17)

Chapter 4

4.1 Introduction

Plasma source ion implantation technique was used to implant mild steel samples *(0.25%C)* with nitrogen ions. In the first part of this study a small sample was implanted with nitrogen ions and the uniformity of the implanted dose was measured from one edge of the sample to another. In the second part of this study the effect of the pulse repetition was investigated. The samples were mounted flush inside a much larger holder see figure 4.1. Both the extended target holder and samples were implanted. No edge effects were expected here and different pulsing frequencies were used.

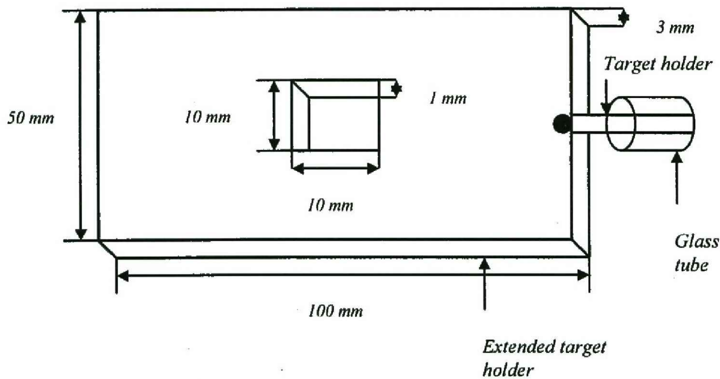

Figure 4.1: Diagram represents an extended stainless steel target holder, design to hold 10x10 mm mild steel samples (P_2 and P_3).

4.2 Sample geometry and treatment specification

Mild steel (*0.25%*C) sample P_1 of the following dimensions *(20.3 mm wide and 29.7 mm long)* was used. Sample P_2, P_3 both *10 mm* wide and *10 mm* long were used in this study. See figure 4.2 below. Typical PSII conditions for sample P_1 are as follows: chamber pressure $8x10^{-4}$ *mbar*, filament bias of *60 V*, discharge current *1.5 A*, pulse width of *10 μs* and for sample P_2 and P_3 base pressure was the same as that of sample P_1, however the filament bias for sample P_2 and P_3 was *50 V*, discharge current was *1 A*, pulse width *5 μs* and the biased voltage was *20 kV*. See implantation parameters and typical retained dose calculated by netlab software on Table 4.1. Two unimplanted samples were used as control.

Table 4.1: Implantation parameters explored.

Sample	*Energy (kV)*	*Frequency (Hz)*	*Average Current (mA)*	*Duration (minutes)*	*Dose ions/cm²*
P_1	20	600	≈10	140	$8x10^{17}$
P_2	20	250	≈8	191	$4x10^{16}$
P_3	20	500	≈12.5	118	$3x10^{16}$

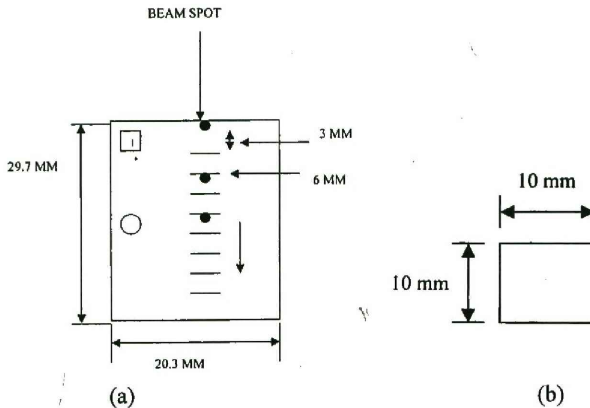

Figure 4.2: Schematic diagram of (a) the sample identified as P_1. It also indicates the beam spot (1 mm) separated 3 mm apart. (b) Depict sample P_2 and P_3 that are the same in size, were used for investigating the effect of pulse repetition rate during ion implantation process. They were mounted inside a holder 50x100x3 mm.

4.3 Investigation of dose distribution

A steel sample designated P_1 was placed inside the plasma chamber to be implanted with nitrogen. Since the sample was small it was much easier for it to heat up and to allow nitrogen ions to diffuse into a sample. The sample was subjected to the following implantation conditions: frequency *600 Hz*, biasing voltage *20 kV*, duration *140 minutes* and the retained dose of $8x10^{17}$ $ions/cm^2$. Retained dose was calculated using mean current of approximately *10 mA* and secondary electron coefficient (γ) by netlab software, utilizing equation (3-1). The intention was to determine retained dose distribution across sample P_1.

4.3.1 RBS measurements

Platinum on silicon (Pt/Si), silicon dioxide on silicon (SiO_2 /Si) and gold on silicon (Au/Si) were used as standards for energy calibration and the table below depicts the energy and the channel for each element.

Table 4.2: Shows the values for energy and channel for each element used as energy calibration standards for sample P_1.

Elements	*Channel*	*Energy (keV)*
Pt	*437.1*	*1845*
Si	*259.0*	*1138*
O	*158.1*	*731.8*
Si	*259.5*	*1138*
Au	*437.0*	*1846*

The following Figure 4.3 shows the straight line fit through the data while Figure 4.4 shows spectra of those standards.

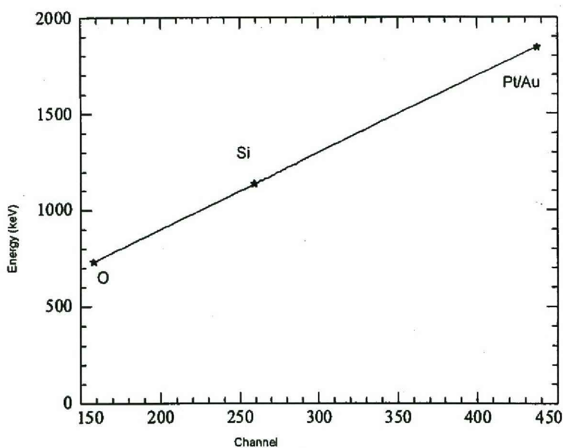

Figure 4.3: Depict the points of the elements and the values for the slope and offset were 3.988 +/- 0.007 and 103 +/- 2

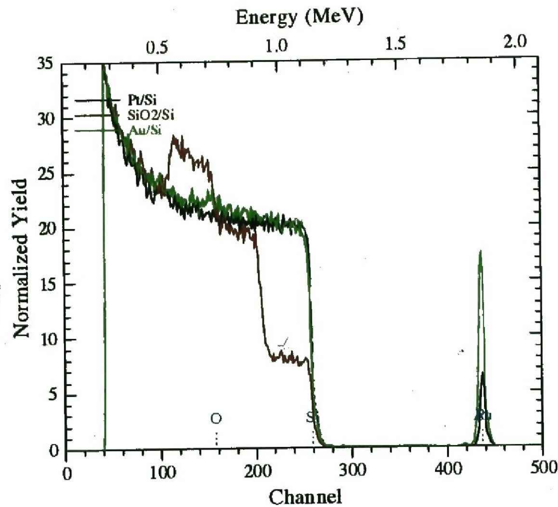

Figure 4.4: Shows the spectra for the standards as overlaid to each other.

Rutherford backscattering spectrometry measurements were performed. A mild steel sample was irradiated at the center by alpha beam as incident particles at energies *2.00 MeV* and detection angle was 170^0. The incident beam, sample normal and also the scattered beam directed at the detector were all in the same horizontal plane and the setup is called IBM geometry. Another unimplanted mild steel sample of exactly the same dimensions was used to act as a control. However as seen in Figure 4.5, it was found that nitrogen was present underneath the surface of sample P_1.

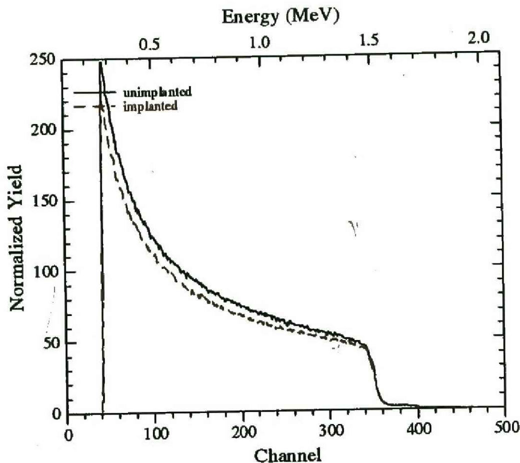

Figure 4.5: Shows RBS spectrum for the implanted sample P_1 is identified by dash line while for unimplanted sample (control) by solid line.

The spectra show that there is a reduced amount of iron (Fe) in the implanted sample P_1 as compared to the unimplanted target (control) and this indicates the presence of nitrogen in the sample. Simulation performed to the implanted sample reveal that iron nitrogen is present at least in the first *450 nm* of steel. Nitrogen could be even deeper, but the experimental setup, only probe the first *450 nm* of steel.

4.3.2 NRA measurements

Sample P_1 was examined using nuclear reaction analysis (NRA). A TiN sample of thickness between *500* and *2500 μg/cm²* was used as a standard for energy calibration [Pro94]. A deuterium beam of energy 1.2 MeV as incident particle was irradiated onto the sample in steps of 3 mm from one edge to the other and the beam spot was *1mm* (see figure 4.2). The detection angle of the NRA products was 150^0 with respect to the incoming beam. A *13 μm thick* mylar foil *($C_{10}H_8O_4$)* was placed in front of the detector to

stop the scattered deuteron beam and to protect the detector from being damaged by the scattered deuteron beam. Cross section chosen were in-line with the cross sections from SIMNRA database especially for the nuclear reaction of interest (See Figure 4.6). However, the cross-section for $^{14}N(d,p_3)^{15}N$ had to be reduced by a factor of *5*, as it seems that the data was not correctly scaled in SIMNRA as well as sigmabase.

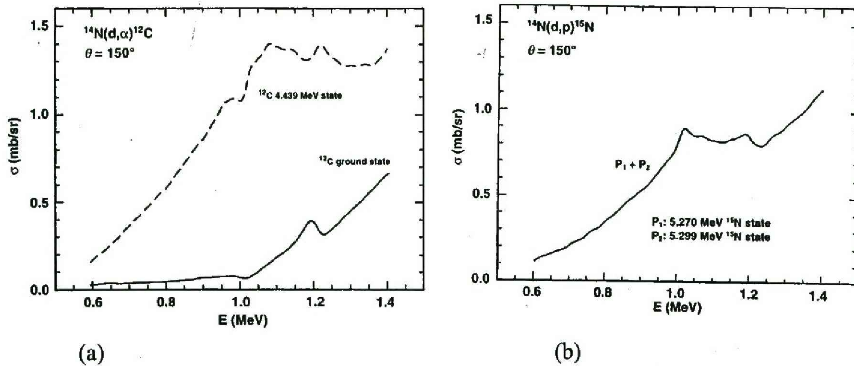

Figure 4.6: (a) The $^{14}N(d,\alpha)^{12}C$ reaction measured at $\theta = 150^0$ from 0.6 to 1.4 MeV (α_0 and α_1) from G. Amsel, D. David. (b) The $^{14}N(d,p)^{15}N$ reaction measured at $\theta = 150^0$ from 0.6 to 1.4 MeV. (c) Shows $^{14}N(d,p_3)^{15}N$ reaction cross-section at $\theta = 150^0$ and the p_3, p_4 and p_5 states [Ams69].

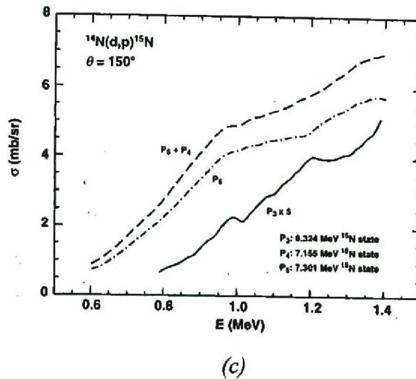

(c)

All nuclear reactions of interest were identified in sample P_1, see figure 4.7. The spectrum identified by a red colour for unimplanted sample (control), depict high carbon content, which was probably due to some surface contamination of the unimplanted sample.

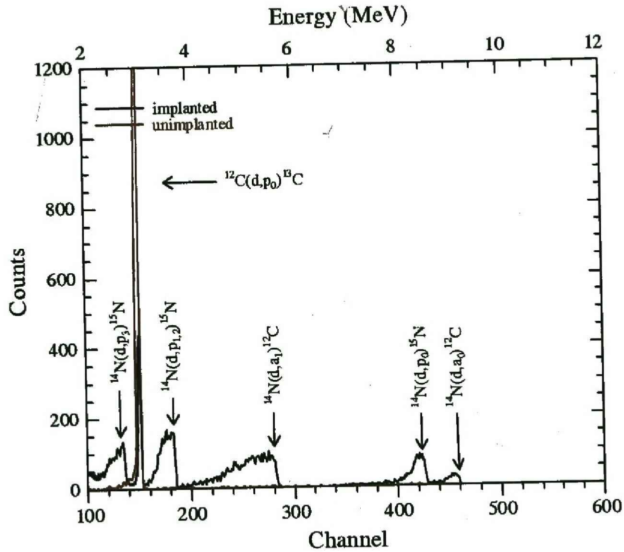

Figure 4.7: NRA spectrum showing the implanted and the unimplanted nuclear reaction peaks.

4.3.3 Distribution profile

By simulation using SIMNRA program the following nuclear were identified as shown on figure 4.8. From right to left there's $^{14}N(d,a_0)^{12}C$ reaction which is shown by a small broad peak followed by $^{14}N(d,p_0)^{12}C$, $^{14}N(d,a_1)^{12}C$, $^{14}N(d,p_{1,2})^{15}N$, $^{12}C(d,p_0)^{13}C$

and $^{14}N(d,p_3)^{15}N$. Moreover SIMNRA reveal that iron nitride thickness in sample P_1 was $10.2\times10^{18}\ atoms/cm^2$, and by estimating the alloy density using iron density $(8.5\times10^{22}\ atoms/cm^3)$ a thickness of about 1.2 μm was calculated.

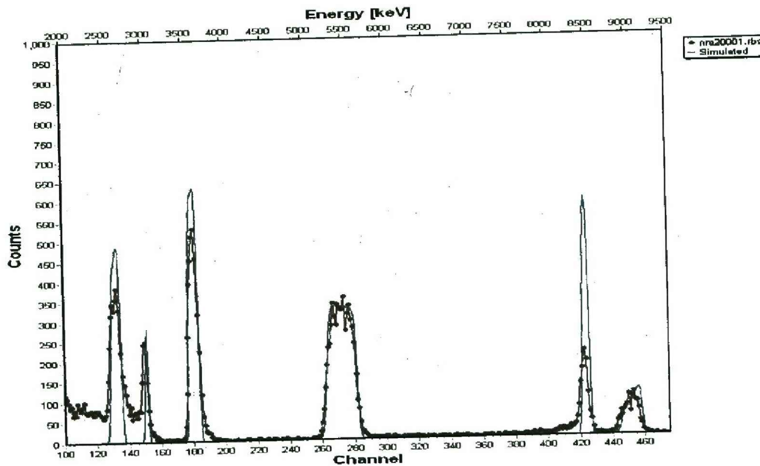

Figure 4.8: Shows simulated spectrum for the implanted sample, the blue line is the simulation line and the red line indicates the experimental spectrum.

Table 4.3: Show the counts for different nuclear reactions from the center in millimeters as indicated by figure 4.9 for the implanted sample. The relative amount of nitrogen is calculated with respect to the amount at the center of the sample.

Distance from center (mm)	*Counts* $^{14}N(d,p_{1,2})^{15}N$	*Relative amount*	*Counts* $^{14}N(d,\alpha_1)^{12}C$	*Relative amount*	*Counts* $^{14}N(d,p_0)^{15}N$	*Relative Amount*	*Counts* $^{14}N(d,\alpha_0)^{12}C$	*Relative amount*
-11.85	2109	0.74	3319	0.73	1028	0.71	294	0.89
-8.85	2512	0.88	3761	0.83	1164	0.81	304	0.92
-5.85	2726	0.95	4307	0.95	1376	0.95	332	1
-2.85	2831	0.99	4463	0.98	1425	0.99	320	0.96
0.15	2845	1	4536	1	1441	1	304	0.92
3.15	2819	0.99	4484	0.99	1334	0.93	311	0.94
6.15	2740	0.96	4337	0.96	1239	0.86	307	0.93
9.15	2351	0.82	3669	0.81	1148	0.79	298	0.89
12.15	1779	0.63	3011	0.66	908	0.63	250	0.75

The values represent the graph shown on Figure 4.9 below. Sample P_1 was irradiated by deuteron beam, from the edger to the center step-wise. See figure 4.2. The results were taken by integrating the counts for each nuclear reaction peak and divided by the highest counts for each nuclear reaction peak at different locations, bombarded by the beam to represent the counts as relative thickness.

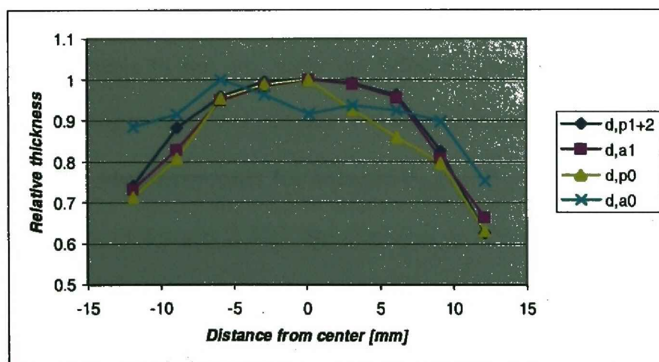

Figure 4.9: Presents counts as relative thickness versus distance from the center to the edge.

The graph shows that there's a lower yield of nitrogen on the edge than on the center. Lines connecting square, cross and triangle figures identify various nuclear reactions at various position on the sample from the center to the edge. The center of the sample represented by zero on the x-axis indicates that there is a higher yield of nitrogen at the center than on the edges.

4.4 Effect of pulse repetition rate

Target holder capable of accommodating a sample of the following dimensions *10 mm* wide and *10 mm* long was design and constructed. The holder was a stainless steel of the following dimensions *50 mm* wide, *100 mm* long and *3mm* in height, and it was also connected to another rod like target holder covered by a glass tube. A square shaped hole of this dimensions *10 mm* wide, *10 mm* long and *1mm* in height was constructed in the center of the target holder to accommodate the sample see figure 4.1. Sample P_2 and P_3 were mounted by a silver paint in that target holder, one at a time during ion implantation. Sample P_2 was subjected to the following implantations parameters: frequency *250 Hz*, biasing voltage *20 kV*, duration *191 minutes* and retained dose $4x10^{16}$ $ions/cm^2$. Sample P_3 was also under the following implantation parameters: frequency *500 Hz*, biasing voltage *20 kV*, duration *118 minutes* and retained dose $3x10^{16}$ $ions/cm^2$.

4.4.1 RBS measurements for sample P_2 and P_3

Helium beam of energies *2 MeV* was employed and the detection angle was $\theta = 170^0$. The target normal to the beam followed IBM geometry of theta *–10*, phi *15* and psi *5*. Energy calibration was done similar to section 4.3.1.It was found to be *4.040+/- 0.003* for slope and *116 +/- 9*.Simulated spectra done using Rump program indicate that at *500 Hz* nitrogen can penetrate into the sample as far as *0.09 μm* and at *250 Hz* nitrogen can go

through as far as *0.05 μm*. Small tantalum peak was identified and it was due to contamination of plasma chamber from tantalum filament used as a glow discharge material See figure 4.10.

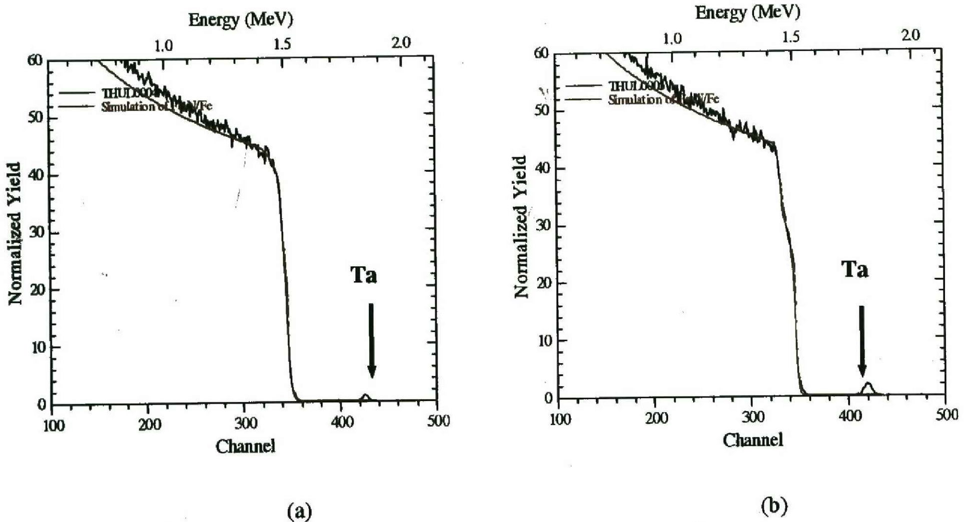

Figure 4.10: (a) Shows RBS simulated spectrum for implanted sample P_2 at 250 Hz and ion depth was 0.05 μm. (b) Also RBS simulated spectrum for implanted sample P_3 at 500 Hz and the ion depth was 0.09 μm.

4.4.2 NRA measurements for sample P_2 and P_3

Standards used for energy calibration were similar to the one used in section 4.3.2 Investigations were done for the effect of pulse repetition rate during ion implantation and at *250 Hz* for sample P_2 simulation results by SIMNRA indicate that iron nitride thickness was about *0.09 μm* and for sample P_3 at *500 Hz* iron nitride thickness was

approximately *0.1 μm* and three nuclear reactions peaks of interest $^{14}N(d,a_0)^{12}C$, $^{14}N(d,a_1)^{12}C$ and $^{14}N(d,p_{1,2})^{15}N$ were identified, see figure 4.11

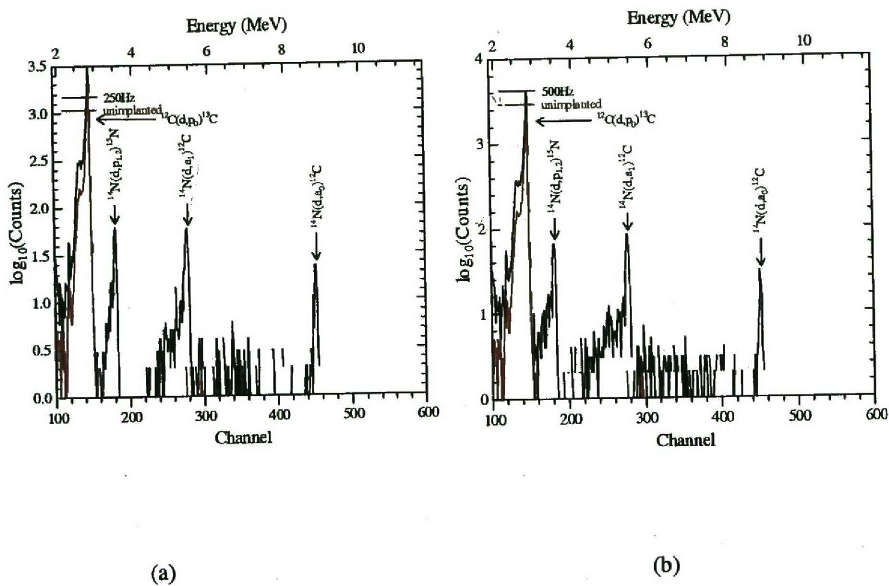

Figure 4.11: (a) NRA spectrum showing nuclear reaction peaks for implanted sample P_2 at 250 Hz. (b) NRA spectrum indicating implanted sample P_3 at 500 Hz.

Chapter 5

5.1 Conclusion

The depth of nitrogen in sample P_1 *(1.2μm) see section 4.3.3* is far greater than sample P_2 and P_3, which was found to be *0.09 μm* for sample P_2 and *0.1 μm* for sample P_3. Results were obtained by using NRA technique. The great depth in sample P_1 must therefore be due to elevated workpiece surface temperature, because sample had a very small mass and during implantation it get heated up and nitrogen ions diffuse into the sample. A rough approximation of the temperature rise of a sample is given by [Fun00]:

$$\Delta T \approx \frac{I_{total} V_p \tau_p f_p t_{impl}}{(1+\gamma_{SE}) M_t c_p} \tag{5-1}$$

Where ΔT is the expected temperature rise of the workpiece in (kelvins), I_{total} is the ion and the secondary electron current in (amperes), V_p is the pulsed voltage applied to the workpiece (volts),τ_p is the length of voltage pulse (seconds), f_p is the pulse repetition rate (pulses per second), t_{impl} is the total implantation time (seconds), γ_{SE} is the secondary electron emission coefficient, M_t is the total workpiece mass (kilograms) and c_p is the workpiece specific heat (joules per kilograms kelvins). Sample P_2 and P_3 were embedded in a bigger block (extended target holder) see figure 4.1, did not heat up as much as sample P_1, and they portrayed shallower nitrogen penetration. SRIM program was utilized to give an insight on how nitrogen ions of particular energies (20 keV) are distributed into steel. Mean ion range was found to be 0.24 μm (Figure 3.7) after running SRIM program. Sample P_2 at 250 Hz shows a little depth of nitrogen ions (0.09 μm) as compared to sample P_3 at 500 Hz (0.1). The higher pulse rate the greater the ion penetration into the material. NRA was useful for

comparative studies as compared to RBS. If edge effects to be studied, then the need for a bigger sample or temperature controlled sample to quantify the effects on much larger sample. Glow discharge method of plasma generation has the following disadvantages:

- possible contamination to the sample
- inert gases cannot be utilized.

5.2 Summary

Plasma Source Ion Implantation technique was used to implant a (*0.25%C*) mild steel sample with nitrogen ions. As stated in chapter 1, the technique has gained increased interest for various applications such as in metal and semiconductor technology. Even though there are surface modification techniques such as surface coating etc. Surface modification by plasma source ion implantation was taken as a suitable technique in this study because of its incredible advantages over conventional beam line implantation. Processes related to ion implantation are as follows, Ion-Beam-Assisted deposition (IBAD), Ion-Beam-Enhanced deposition (IBED) including PSII/PIII, which was employed in this study. Ion implantation as defined on page 8 clearly indicate the need to have a simulation program that will enable the user to compare the ions of interest implanted on a particular material with the one performed experimentally. The program used in this study was monte-carlo code SRIM 2000. The PSII machine used is situated on the first floor of the MRG building as shown on Figure 3.1 and is divided into three essential components, namely RUP-4a pulse generator, vacuum system and the chamber, those components perform their task separately but collectively they perform ion implantation and all of those components are very important. PSII system has netlab software, which facilitate better control of

the plasma implantation procedure. Simulation program called SIMNRA was also used to identify the nuclear reactions and give an insight about the depth of nitrogen ions into steel. Figure 4.7 shows simulated spectrum of implanted workpiece, the line identified in blue color is the simulation line that went through peaks of experimental spectra and thus showing the nuclear reaction peaks of interest.

5.3 Future Work

- Investigate the microhardness of steel material using AFM technique.
- Develop or install RF plasma generating facility.
- Implantation of polymer material.

Appendix A

A.1 Sputtering

The sputtering yield is given by [Sig81]:

$$Y = \Lambda F_D(E_0) \tag{A-1}$$

Where Λ is the material factor and contains all the material properties, such as binding energy, then $F_D(E_0)$ is the energy deposited by nuclear processes per unit length at the surface as given by Winterbon, Sigmund and Sonders [Win70]:

$$dE = N S_n(E(x))dx = F_D(x)dx \tag{A-2}$$

Where $S_n(E(x))$ is the energy dependent nuclear stopping which set-aside or ignore electronic energy losses from recoiling target atoms. Thus the energy deposited at the surface by nuclear process is:

$$F_D(E_0) = \alpha N S_n(E_0) \tag{A-3}$$

Where N is the atomic density of the target at the surface, $S_n(E_0)$ the nuclear stopping cross-section at energy E_0 and $N S_n(E_0) = \left.\frac{dE}{dx}\right|_n$ is the nuclear energy loss rate, α is a correction factor, which includes M_1/M_2. The evaluation of $S_n(E)$ depends on the collision cross-section for energy transfer to a substrate atom and the keV sputtering regime and also the electron screening of the nuclear charge must be

taken into account. In order to calculate the sputtering yield Y, nuclear stopping cross-section deposited via nuclear processes must be determined.

A.1.1 Deposited energy

The deposited energy F_D is given by $F_D = \alpha N S_n$, where α is a function of the mass ratio M_2/M_1 and the value of α also increases with the angle of incidence β.

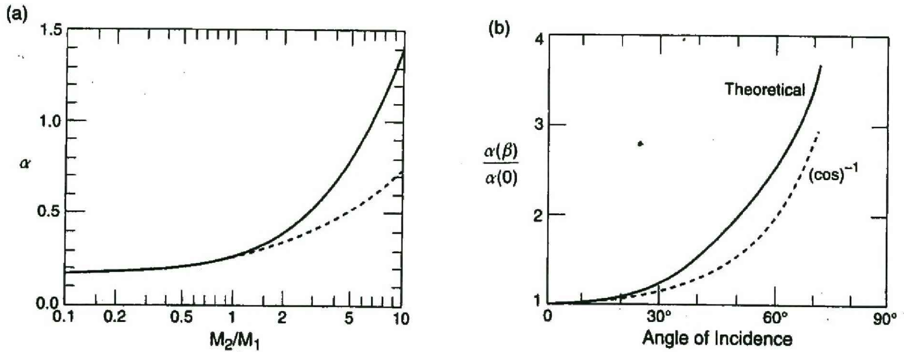

Figure A.1: (a) Factor α as a function of the mass ratio M_2/M_1 and (b) dependence on angle of incidence. Taken from Sigmund 1981.

A.1.2 Sputtering yield

The material factor Λ contain the material parameter and describes the number of recoil atoms that can escape from the solid and is given by (Sigmund 1981):

$$\Lambda \cong 4.2 / N U_0 \; nm/eV \qquad \text{(A-4)}$$

Where N is the atomic density in $(nm)^{-3}$ and U_0 is the surface binding energy in electron volts. U_0 can be estimated from cohesive energy given by Kittel (1976). The sputtering yield is given by:

$$Y \cong 4.2\alpha S_n(E_0) = 4.2\alpha \left(dE/dx\right)_n (NU_0)^{-1} \quad \text{(A-5)}$$

Where N is in $(nm)^{-3}$, $NS_n = dE/dx$ is in electron volts per nanometer.

A.2 Semi-empirical formula for sputtering of single elemental targets

Semi-empirical equation for sputtering was developed by Matsunami et al (1984) and Yamamura and Itoh (1989), where-by they combined the Lindhard's theory of nuclear and electronic stopping and also with numerical values of sputtering data. Thus the empirical sputtering yield (Y_E) which take both heavy-ion and light-ion sputtering.

$$Y_E(E) = 0.42 \frac{\alpha_s Q_s S_n(E)}{U_0\left[1 + 0.35 U_0 S_e(\varepsilon)\right]}\left[1 - (E_{th}/E)^{0.5}\right]^{2.8} \quad \text{(A-6)}$$

Where $Y_E(E)$ is the sputtering yield for ions with energy E at normal incidence. α_s and Q_s are empirical parameters determined from experimental sputtering data, E_{th} is the sputtering threshold energy, $S_e(\varepsilon)$ is the reduced Lindhard electronic stopping cross-section, $S_n(E)$ is the nuclear stopping cross-section in units of 10^{-15} eV cm^2, and U_0 is the surface binding energy which can be estimated from the cohesive energy. The sputtering threshold energy can be calculated:

$$E_{th} = \left\{\left(\frac{4}{3}\right)^6 \frac{U_0}{\gamma} \qquad M_1 \geq M_2 \quad \text{(A-7)}\right.$$

$$E_{th} = \left\{\left(\frac{2M_1 + 2M_2}{M_1 + 2M_2}\right)^6 \frac{U_0}{\gamma} \qquad M_1 < M_2\right.$$

The equation above shows the approach by Yamamura and Itoh (1989) for calculating the sputtering threshold energy. Where γ is the energy-transfer factor for elastic collision defined below:

$$\gamma=\frac{4M_1 M_2}{(M_1+M_2)^2} \tag{A-8}$$

In fitting the experimental data, the following analytical approximation to Lindhard's reduced nuclear stopping cross-section was employed:

$$S_n(E)=K_n S_n(\varepsilon) \tag{A-9}$$

Where $K_n=\frac{8.478 Z_1 Z_2}{\left(Z_1^{2/3}+Z_2\right)^{1/2}}\frac{M_1}{(M_1+M_2)}\left(10^{-15}\, eV\, cm^2/atom\right)$ (A-10)

And $S_n(\varepsilon)=\frac{3.441\varepsilon^{1/2}\ln(\varepsilon+2.718)}{1+6.355\varepsilon^{1/2}+\varepsilon\left(6.882\varepsilon^{1/2}-1.708\right)}$ (A-11)

The reduced energy ε is given by: $\varepsilon=\frac{0.03255}{Z_1 Z_2\left(Z_1^{2/3}+Z_2^{2/3}\right)^{1/2}}\frac{M_1}{(M_1+M_2)}E(eV)$ (A-12)

The best fit values for the sputtering parameters α_s and Q_s were obtained by fitting Eq. (A-11) to experimental data, and values of α_s was found to be dependent on each ion-target combination and the following empirical expression was obtained:

$$\alpha_s=0.10+0.155(M_2/M_1)^{0.73}+0.001(M_2/M_1)^{1.5} \tag{A-13}$$

The parameter Q_s was found to depend only on the target material and its values are listed in Table A.1 along with U_0 values.

Table A.1 Q_s values together with cohesive energy values U_0, taken from [Nas96]

Target	Z	U_0(eV)[a]	Q_s[b]
Be	4	3.32	1.97
B	5	5.77	4.1
C	6	7.37	2.69
Al	13	3.39	1.11
Si	14	4.63	0.95
Ti	22	4.85	0.58
V	23	5.31	0.76
Cr	24	4.10	1.03
Mn	25	2.92	1.09
Fe	26	4.28	0.9
Co	27	4.39	0.98
Ni	28	4.44	0.94
Cu	29	3.49	1.27
Ge	32	3.85	0.73
Zr	40	6.25	0.68
Nb	41	7.57	1.02
Mo	42	6.82	0.70
Ru	44	6.74	1.51
Rh	45	5.75	1.23
Pd	46	3.89	1.09
Ag	47	2.95	1.24
Sn	50	3.14	0.58
Hf	72	6.44	0.65
Ta	73	8.10	0.62
W	74	8.90	0.77
Re	75	8.03	1.34
Os	76	8.17	1.47
Ir	77	6.94	1.39
Pt	78	5.84	0.93
Au	79	3.81	1.02
Th	90	6.20	0.73
U	92	5.55	0.66

A.3 Sputtering at glancing angles

Eq. (A-11) is a semi-empirical sputtering formula for monatomic solids irradiated at normal incidence. However when the projectile ion is incident at glancing angles. The sputtering yield differs from the normal incidence yield and it is observed that in general the sputtering due to a projectile ion at an incident angle β is related to Y (0) as shown by:

$$Y(\beta)=(\cos)^{-f_s}\cdot Y(0) \qquad \text{(A-14)}$$

Where β is measured from the surface normal and f_s is a function of M_2/M_1. For light-ion sputtering where values of $(M_2/M_1 > 10)$, f_s can be estimated by (Yamamura and Itoh, 1989):

$$f_s = 1 + (\Delta R_{p_x} / \Delta R_{p_y})^2 \qquad \text{(A-15)}$$

Where ΔR_{p_x} and ΔR_{p_y} are the ion-range straggling in the direction of the ion and perpendicular to the ion trajectory respectively. For large mass ratios,

$\left(\Delta R_{p_X} / \Delta R_{p_Y}\right)^2 \cong 1$ and $f_s \to 2$. For heavy-ion sputtering where values of $(M_2/M_1 < 10)$, f_s can be approximated by:

$$f_s = 1 + \left(\frac{\langle Y^2 \rangle_D}{\langle \Delta X^2 \rangle_D} \frac{\langle X \rangle_D^{\ 2}}{\langle \Delta X^2 \rangle_D} \right) \quad \text{(A-16)}$$

Where $\langle X \rangle_D$ is the average depth of damage and $\langle Y^2 \rangle_D^{\ 1/2}$ and $\langle X^2 \rangle_D^{\ 1/2}$ are the damage straggling in the direction of the ion perpendicular to ion direction. For values of $M_2/M_1 < 1$, the ratios $\langle \Delta X^2 \rangle_D / \langle X \rangle_D^{\ 2}$ and $\langle Y^2 \rangle_D / \langle X \rangle_D^{\ 2}$ are nearly constant with average values of approximately 0.4 and 0.15 respectively using these values in Eq. (A-16) gives $f_s \cong 1.9$

A.4 Ion implantation and the steady state condition

During ion implantation, the sputtering process removes both target and implanted atoms, Eventually an equilibrium condition or steady state is reached, where-by just as many ions are removed by sputtering as are replenished by implantation. The depth distribution under this condition has peak at the surface, however drops off with depth according to the ion range seen on figure A.2:

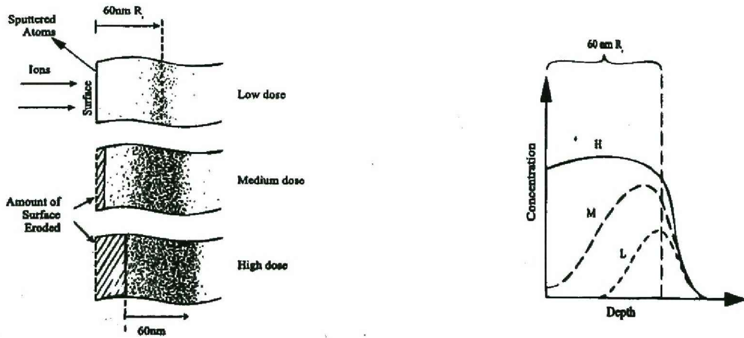

Figure A.2: Schematic view of the development of the concentration profile of ions implanted from low to high doses and the implantation depth profiles for low to high doses, R_p is 60 nm.

The steady state surface condition is calculated this way, consider the implantation of ion species A into the host material B, then let N_A and N_B be the concentrations (per unit volume) of A atoms and B atoms at the sample surface. The surface composition is given by N_A / N_B, then let J_A and J_B be the flux of the sputtered atomic species A and B. Thus J_B / J_A gives:

$$J_B / J_A = r(N_B / N_A) \quad \text{(A-17)}$$

Where r is the ratio of the probability for B atom near a surface to be sputtered to that of an A atom to being sputtered. Then flux of incident ions of species A is defined as J_i and the total sputtering yield Y as:

$$(J_A + J_B) = YJ_i \quad \text{(A-18)}$$

At steady state, there is no transformation in the total number of A atoms in the material, therefore

$$J_A = J_i \quad \text{(A-19)}$$

And by combining Eq. (A-18) and (A-19) we obtained:

$$J_B = (Y-1)J_i \quad \text{(A-20)}$$

And also by substituting (A-19) and (A-20) into Eq. (A-17) we obtained:

$$N_A / N_B = r(Y-1)^{-1} \quad \text{(A-21)}$$

Hence the steady state surface composition and it is roughly inversely proportional to the yield Y, but is multiplied by the preferential sputtering factor r.

A.5 Sputtering of alloys and compounds

Sputtering process in alloys and compound is based on the collision cascade picture, this theory is explained by [Sig81]. Actually the incident ion initiates collisions in a volume surrounding the ion track. Thus the energy of the incident ion is shared among those atoms within that volume and is then dissipated, and then collisions that take place near the surface of the material are directly effective in knocking atoms out of the material. The main features remain the same for composite materials such as

binary alloys, however there are additional complications because there are two kinds of atoms in the material. The two species may not sputter at an equal rate because of difference in energy sharing, ejection probabilities or binding energies.

A.5.1 Preferential sputtering

Sputtering as described from multi-components system, involves preferential sputtering and surface segregation. Then for a homogenous sample with two atomic components A and B, the surface concentration, N^s are equal to those in the bulk N^b, and then the pre-sputtered composition has

$$N_A^s / N_B^s = N_A^b / N_B^b \qquad \text{(A-22)}$$

The partial yield of atomic species A and B is given as follows:

$$Y_{A,B} = \frac{\textit{number of ejected atoms } A,B}{\textit{incident particle}} \qquad \text{(A-23)}$$

The ratio of partial yields is given as:

$$\frac{Y_A}{Y_B} = r\frac{N_A^s}{N_B^s} \qquad \text{(A-24)}$$

Where the sputtering factor r, accounts for differences in surface binding energies, sputter escape depth and the energy transfers within the cascade. Measured values of r range from 0.5 to 2. For $r \neq 1$ the surface yield and concentrations will transform from initial values, $N_A^s(0)$ and $Y_A(0)$ to the steady state values of $N_A^s(\infty)$ and $Y_A^s(\infty)$.

Thus at t = 0 gives:

$$\frac{Y_A(0)}{Y_B(0)} = r\frac{N_A^b(0)}{N_B^s(0)} = r\frac{N_A^b}{N_B^b} \qquad \text{(A-25)}$$

If there is preferential sputtering where $r > 1$, the sputtering yield of A is greater than that of B and result in the surface enriched in B. The enrichment of the surface produces an increase in the sputtering yield of B and a decrease in the sputtering yield

of A, however under steady state condition the processes are balanced as the surface erodes into the bulk and the surface concentration differs from the bulk according to:

$$\frac{N_A^s(\infty)}{N_B^s(\infty)}=\frac{1}{r}\frac{N_A^b}{N_B^b} \tag{A-26}$$

A.5.2 Composition Changes

Considering process such as steady-state sputtering and preferential sputtering, surface composition can be affected. This is true in surface modification applications; especially where high dose implants are used to form modified surface alloys. Then these changes in surface composition of sputtered multi-component targets are well documented by Betz and Wehner [Bet 83].

A.5.3 Composition depth profiles

Ion implantation automatically alter the composition of the surface material, then one expects composition profiles to vary and for changes in composition to extend to the range of the implanted ion. Thus the ability of plasma implantation techniques to implant required doses can be severely limited if the steady-state composition occurs before desired implantation composition is reached. However thermal diffusion and radiation-enhanced diffusion can promote diffusion of the implanted projectile to greater depths. A detailed discussion of sputtering composition depth profiles is given by Bertz and Whener [Bet83].

A.6 High dose ion implantation

Atomic mixing, sputtering, and chemical effects tend to be essential in determining the state of the material in high-dose implantation. In general the maximum

implantable concentration is limited by the reciprocal of the sputtering yield (A-1). This occurs because of the surface receding due to sputtering and the sputter removal of implanted ions. The maximum concentration is therefore established after a thickness comparable to the ion range has been removed. Sputter processes should be taken into cognizance if there is preferential sputtering of the implanted ion. Based on assumption that atomic mixing is very efficient such that, after an initial dose of about $10^{16}\ atoms/cm^2$, the implanted species spread uniformly over the effective depth R_p and also assuming the shape of the profile remain constant, but with its amplitude increasing with further implantation. The steady state erosion can be given as follows. The conservation of atoms requires:

$$R_p \frac{dN_A}{dt} = J_i - J_A \tag{A-27}$$

Where N_A is the concentration of the implanted species, J_i is the projectile flux, J_A is the flux of the sputtered A atoms, J_A, J_B and J_i are related according to equations (A-17) and (A-18). By defining $x \equiv N_A/N_B$ and assuming Y remain unchanged then equations (A-17) and (A-18) give

$$J_A = \frac{x}{r+x} Y J_i \tag{A-28}$$

$$J_B = \frac{r}{r+x} Y J_i \tag{A-29}$$

Substituting equations (A-28) and (A-29) into equation (A-27) gives:

$$R_p \frac{d}{dt}\left(\frac{x}{1+x}\right) N_0 = J_i - \frac{x+r+x}{Y} J_i \tag{A-30}$$

Where $N_0 \equiv N_A + N_B$ after some rearrangement, equation (A-30) becomes

$$\frac{r+x}{(1+x)^2 \left[r + (1+Y)x\right]} dx = \frac{1}{N_0 R_p} (d\phi_A) \tag{A-31}$$

Where $d\phi_A \equiv J_i\, dt$ is the incremental ion dose. Eq. (A-31) is a differential equation for $x(\phi_A)$, which is solved by taking partial fractions for the left hand side and integrating to get:

$$Y\left[\frac{Ax}{1+x}+B\ln\left(\frac{1+x}{1-x/x(\infty)}\right)\right]=\frac{Y\phi_A}{N_0\,R_p} \qquad \text{(A-32)}$$

Where $A\equiv(r-1)/[r-(1-Y)]$, $B\equiv Yr/[(1-Y)-r]^2$ and $x(\infty)=r/(Y-1)$. The expression $Y\phi_A/N_0\,R_p$ can be interpreted as the amount of material sputtered as measured by the thickness of the implanted layer. The steady state composition is the same as predicted by Eq. (A-26). The amount of material to be eroded before steady state condition are reached and defined as follows:

$$\phi_0=\frac{x(\infty)}{(dx/d\phi_A)_{\phi_A=0}} \qquad \text{(A-33)}$$

Which is the dose required to achieve steady state. Equation (A-31) gives

$$\left.\frac{dx}{d\phi_A}\right|_{\phi_A=0}=\frac{1}{N_0\,R_p} \qquad \text{(A-34)}$$

Since $s(\infty)=r(Y-1)^{-1}$ equations (A-32) and (A-34) gives

$$(Y-1)\phi_0=r(N_0\,R_p) \qquad \text{(A-35)}$$

For Y>> 1 gives

$$\frac{Y\phi_0}{N_0\,R_p}\cong r \qquad \text{(A-35)}$$

A.7 Factors that influence concentration in high dose ion implantation

Since most of sputtered atoms have relatively low energies and emerge from the first few atomic layers near the surface. A thin oxide layer or other surface contaminant

can reduce the sputtering yield and therefore protect the surface, but because of ion mixing which causes the surface contaminant to be mixed into the modified layer hence surface contaminants may be a source of significant detrimental side-effects. The surface layer is influenced by several factors such as residual gas in a bad vacuum, the target material, and the current density of the incident ion beam. Sputtering can also give rise to surface roughness, which can possibly affect the high dose implantation. An extremely rough surface can reduce the sputtering yield. Backscattering measurements of depth distributions have revealed low retained doses near surface regions even without sputtering. This implies that inert-gas ions can escape from the target material, reducing surface concentration.

A.8 Sputtering Spike

Sigmund model [Sig81] assume that the collision cascade produced by the projectile is linear and could be estimated by binary collisions, but if the projectile energy results in a mean free path between displaced target atoms approaching atomic lattice spacing the binary collision approximation breaks down under such conditions. The energy is dissipated over a very short distance, producing effective temperatures at the surface that can exceed the melting and vaporization temperature of the material. These conditions are called Spike regime and anomalous high sputtering yield can be approximated by assuming that the atoms in the spike behave as an ideal gas, this assumes that the surface atoms have a Maxwellian velocity distribution from which a mean velocity can be calculated and which in turn can be used to approximate an evaporation rate from spike surface area. It can be shown from the kinetic theory of gases that the one-dimensional velocity distribution of atoms of mass M_2 at a temperature T is given by:

$$f(v_x)=\left(\frac{M_2}{2\pi k_B T}\right)^{\frac{1}{2}} e^{\frac{-1/2 M_2 V_x^2}{k_B T}} \tag{A-36}$$

Where k_B is Boltzmann's constant. The average velocity is then given by

$$\langle v_x \rangle = \int_0^\infty v_x f(v_x) dv_x$$

$$= \left(\frac{M_2}{2\pi k_B T}\right)^{\frac{1}{2}} \int_0^\infty v_x e^{\frac{-1/2 M_2 v_x^2}{k_B T}} dv_x$$

$$= \left(\frac{k_B T}{2\pi M_2}\right)^{1/2} \tag{A-37}$$

Taking the activation energy for evaporation in the surface binding energy U_0, the rate of evaporation, J_e per unit time and unit area at the surface temperature, T_{surf}, is given by Sigmund [Sig81] as:

$$j_e \cong N \langle v_x \rangle e^{-U_0/k_B T_{surf}}$$

$$\cong N \left(k_B T_{surf} / 2\pi M_2\right)^{\frac{1}{2}} e^{-U_0/k_B T_{surf}} \tag{A-38}$$

Where N is the target atomic density. The spike surface temperature, T_{surf}, can be related to the average deposited damaged energy at the surface, $\bar{\theta}_{surf}$, through the expression:

$$\bar{\theta}_{surf} = \frac{3}{2} k_B T_{surf} \tag{A-39}$$

The mean deposited damage energy at the surface, $\bar{\theta}_{surf}$, can be calculated from the

expression:

$$\bar{\theta}_{surf} = \frac{(0.68)^2 S_n(E)_{surf}}{A_{cas}} \tag{A-40}$$

Where $S_n(E)$ is the nuclear stopping cross-section and A_{cas}^{surf} is the cascade surface area emitting J_e atoms/cm^{2}s. By assuming that the spike can be estimated by a cylinder at the surface, the surface, the cascade area is given by:

$$A_{cas}^{surf} = \delta_{corr}^{\ 2} A_T = \delta_{corr}^{\ 2} \left(\pi \langle Y^2 \rangle_D \right) \qquad \text{(A-41)}$$

Where A_T is the transport cascade area and calculated either using transport theory or average of many Monte- Carlo histories. The transport cascade radius is taken as the perpendicular distance from the ion trajectory of the ion damage straggling $\langle Y^2 \rangle_D^{1/2}$. The variable δ_{corr} is the cascade volume correction factor relating the transport cascade area to the individual cascade area. The factor $(0.68)^2$ accounts for the fraction of the energy damage residing within a standard deviation of the damage distribution (see section 7.11.4) [Nas96]. For a spike of lifetime τ, the sputtering yield is given by:

$$Y_{spike} = \tau A_{cas}^{surf} J_e \qquad \text{(A-42)}$$

Appendix B

Sheath Theory

During the plasma implantation process high negative voltages are applied to the PSII target, initially on the time scale of the electron plasma period $\left(w_{pe}^{-1}\right)$, electrons near the surface are driven away, leaving behind a uniform density ion matrix sheath, then on the time scale of the ion plasma period $\left(w_{pi}^{-1}\right)$ ions within the sheath are accelerated into the target. This in turn drives the plasma edge away, exposing new ions that are then extracted. Thus the rate of electron loss to any object in plasma is greater than the rate of ion loss, leaving the workpiece with a net negative potential. The electric field of this potential does not penetrate far into the plasma since Debye shielding restricts it to a size of the order of a few Debye length λ_D $\left(\lambda_D = \sqrt{\frac{\varepsilon_0 k T_e}{e^2 n_e}}\right)$ hence the region called a sheath. Thus sheaths act to confine the more mobile of the plasma charged species within the plasma to maintain charge neutrality. Sheath acquires a spherical shape independent of the target as observed by Meyer [Mey96]. Then spherical theory is applicable even in the case of PSII where a high voltage is applied to the target. In the absence of the high voltage, the sheath thickness is of the order of the Debye length (λ_D) and hence effectively conforms to the target shape.

B.1 Time scales

There are three time scales of interest in PSII sheath theory:

- The electrons are much more mobile than the ions and react on a timescale of the order of the electron plasma period $\tau_{pe} = \sqrt{\frac{\varepsilon_0 m_e}{n_e q_e^2}}$. When the pulse is first

applied the electrons respond rapidly and are repelled from the target leaving behind ion- matrix sheath.

- On a much longer timescale of the ion plasma period $\tau_{pi} = \sqrt{\frac{\varepsilon_0 m_i}{n_i q_e^2}}$, the ions start to move towards the target. On this timescale the ions are attracted to the target and the plasma sheath grows to cover more ions to maintain the implantation current.
- Third timescale is determined by the pulse width τ_{pulse}. Normally, the sheath would expand outward until it reaches the distance described by the steady state Child Law [Chi11], however in the PSII process the voltage pulse is sufficiently short that the voltage is returned to zero before the steady state sheath forms.

B.2 Dimensionless Co-ordinates

Dimensionless quantities for all the co-ordinates used in the theory are defined as follows:

$\tilde{r} = \frac{r}{\lambda_D}$ Distance

$\tilde{\phi} = \frac{e\phi}{kT_e}$ Potential energy

$\tilde{n}_e = \frac{n_e}{n_0}$ Electron density

$\tilde{n}_i = \frac{n_i}{n_0}$ Ion density (B-1)

B.3 The initial plasma sheath

For potentials close to the plasma potential, the sheath around conductors is of the order of the Debye length λ_D. During PSII pulse, the target potential is much greater than the plasma potential $\left(\phi_p \approx 10\,eV \text{ versus } \phi_{target} \approx -10\,keV \text{ to } 100\,keV\right)$. Hence the formation of the initial plasma sheath under the mentioned conditions. The description on how to establish the thickness of initial sheath is given by Conrad [Con87]. The potential profile is obtained from Poisson's equation:

$$\frac{d^2\phi}{dr^2}+\frac{\alpha}{r}\frac{d\phi}{dr}=\frac{1}{\varepsilon_0}e\left(n_i-n_e\right) \tag{B-2}$$

Where ϕ is the applied pulse potential, n_i and n_e are ion and electron densities and α = 0,1 and 2 for planar, cylindrical and spherical geometries. When the potential is first applied to the electrode, it is assumed that the plasma is of uniform density and $n_0 = n_i = n_e$. For planar geometry the spatial variable r is measured from the surface of the electrode, while for cylindrical and spherical geometries r is the radial distance from the center of the electrode. Substituting for the dimensionless co-ordinates defined by (B-1) into equation (B-2) gives the dimensionless Poisson's equation:

$$\frac{d^2\tilde{\phi}}{d\tilde{r}^2}+\frac{\alpha}{r}\frac{d\tilde{\phi}}{d\tilde{r}}=-\left(\tilde{n}_i-\tilde{n}_e\right) \tag{B-3}$$

During this initial sheath phase, the electron density n_e= 0, and the ion density equal to background density, then equation (B-3) is reduced to:

$$\frac{d^2\tilde{\phi}}{d\tilde{r}^2}+\frac{\alpha}{r}\frac{d^2\tilde{\phi}}{d\tilde{r}}=-1 \tag{B-4}$$

Evaluation equation (B-4) is a subject to the following boundary conditions:

The potential at the electrode position, r_0 must be equal to the applied potential ϕ_0 and

The electric field must vanish at the sheath position, r_s

$$\tilde{\phi} = \tilde{\phi}_0 \equiv \frac{q_e \phi_0}{k T_e} \qquad at \qquad \tilde{r} = \tilde{r}_0 \equiv \frac{r_0}{\lambda_D} \tag{B-5}$$

$$\frac{d\tilde{\phi}}{dr} = 0 \qquad at \qquad \tilde{r} = \tilde{r}_s \equiv \frac{r_s}{\lambda_D} \tag{B-6}$$

Solutions are found using ordinary differential equation techniques and are:

Planar geometry:

$$\tilde{\phi}(\tilde{r}) = -\tilde{\phi}_0 + \tilde{r}_s(\tilde{r} - \tilde{r}_0) + (\tilde{r}_0^2 - \tilde{r}^2)/2 \tag{B-7}$$

Cylindrical geometry:

$$\tilde{\phi}(\tilde{r}) = -\tilde{\phi}_0 + (\tilde{r}_s^2/2)\ln(\tilde{r}/\tilde{r}_0) + (\tilde{r}_0^2 - \tilde{r}^2)/4 \tag{B-8}$$

Spherical:

$$\tilde{\phi}(\tilde{r}) = -\tilde{\phi}_0 + (\tilde{r}_s^3/3)(1/\tilde{r}_0 - 1/\tilde{r}) + (\tilde{r}_0^2 - \tilde{r}^2)/6 \tag{B-9}$$

Expressions for the sheath position are found by setting the potential to zero in equations (B-7), and (B-9). By defining f to be the ratio of sheath radius to electrode radius $f \equiv \tilde{r}_s/\tilde{r}_0 = r_s/r_0$ the results are given as:

Planar geometry

$$(f-1)^2 = 2\tilde{\phi}_0/\tilde{r}_0^2 \tag{B-10}$$

Cylindrical geometry

$$f^2 \ln f^2 - f^2 + 1 = 4\tilde{\phi}_0/\tilde{r}_0^2 \tag{B-11}$$

Spherical geometry

$$2f^3 - 3f^2 + 1 = 6\tilde{\phi}_0\,\tilde{r}_0 \tag{B-12}$$

Rewriting equations (B-10), (B-12) in dimensional units, can be expressed as follows:

Planar

$$r_s = (2\varepsilon_0 \phi_0 / n_0 q_e)^{1/2} \qquad or \qquad r_s(cm) = 1050[\phi_0(volts)/n_0(cm^{-3})]^{1/2} \tag{B-13}$$

Spherical

$$r_s \cong \left(3\varepsilon_0 \phi_0 r_0 / n_0 q_e\right)^{1/3} \qquad or \qquad r_s(cm) \cong 118\left(\frac{\phi_0(volts) r_0(cm)}{n_0(cm^{-3})}\right)^{1/3} \tag{B-14}$$

Plotting equations (B-13) and (B-14), shows the dependence of ion-matrix sheath width on target and plasma, this can be seen in figure B.1:

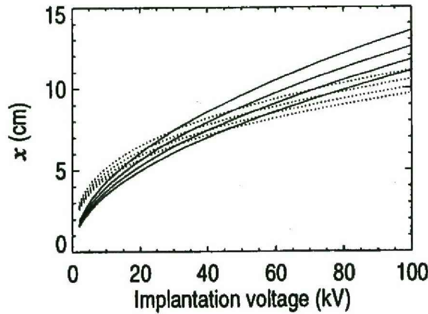

Figure B.1: Dashed line for Planar and solid lines for spherical, this depicts ion-matrix sheath width as a function of target potential for different densities. Spherical calculations use a 10 cm diameter target and the densities (top to bottom) are 6,7,8 and $9 \times 10^{8}\, cm^{-3}$.

B.4 Sheath Evolution

Lieberman [Lie89] proposed one-dimensional planar model describing sheath evolution due to the application of a voltage step $\left[V=0,\ for\ \ t<0, t>t_p\ \ and\ V=-V_0, 0\le t\le t_p\right]$

The model is based on the following assumptions:

- The ion flow is collision less
- Compared to the ions, electron motion inertia less
- The applied voltage V_0 is much greater than T_e, so $\lambda_D << S_0$ and the sheath edge at S is sudden.

- During implantation a quasi-static Child-Law sheath forms.
- The electric field is assumed to remain unchanged for ion motion through the sheath.

Lieberman's model, which solves the Child-Langmuir Law [Lan23] for space charge limited emission quasi-statically was further simplified by Scheuer et al [Sch90]:

$$J = \frac{4\varepsilon_0}{9}\left(\frac{2q_e}{M}\right)^{1/2}\frac{V^{3/2}}{S^2} \qquad \text{(B-15)}$$

Where J is the current density crossing the sheath edge, M is the mass of the ion, V is the magnitude of the applied potential, and S is the distance of the sheath edge from the target. Based on the assumption that

$$j = nq_e\left(\frac{dS}{dt} + v_d\right) \qquad \text{(B-16)}$$

Where v_d is the ion drift velocity, which is equal to the ion acoustic speed, C_s. However assuming that $V_d = 0$, the ions are motionless until the sheath reaches them, then equation (B-15) and (B-16) are solved to give the following:

Planar

$$\frac{ds}{dt} = \frac{4\varepsilon_0}{9n}\left(\frac{2}{q_e M}\right)^{1/2}\frac{V^{3/2}}{S^2} \qquad \text{(B-17)}$$

Which is integrated analytically to yield:

$$S = S_0\left[\frac{2}{3}w_{pi}t + 1\right]^{1/3} \qquad \text{(B-18)}$$

Then if more realistic case of non-motionless plasma is considered, equation (B-17) becomes:

$$\frac{ds}{dt} = \frac{4\varepsilon_0}{9n}\left(\frac{2}{q_e M}\right)^{1/2}\frac{V^{3/2}}{S^2} - v_d \qquad \text{(B-19)}$$

Which is integrated numerically.

In spherical geometries, the Child-Langmuir relation is given as:

$$J=\frac{4\varepsilon_0}{9}\left(\frac{2q_e}{M}\right)^{1/2}\frac{V^{3/2}}{r^2\alpha^2} \tag{B-20}$$

Where α is given by Xia and Chan [Xia93] as $\alpha^2=\gamma^2-0.6\gamma^3+0.24\gamma^4-0.074\gamma^5$,

where $\gamma=\ln\left(\frac{r}{r_0}\right)$, giving the following differential equation for sheath evolution in spherical geometries:

$$\frac{dr}{dt}=\frac{4\varepsilon_0}{9n}\left(\frac{2}{q_e M}\right)^{1/2}\frac{V^{3/2}}{r^2\alpha^2} \tag{B-21}$$

Solution for the ion matrix sheath is presented by Xia and Chan as:

$$R_0\cong(3A)^{1/3}+(1/2) \tag{B-22}$$

Where $A=\frac{q_e V \lambda_D^{\ 2}}{kT_e r_t^{\ 2}}$, then figure B.2 show a comparison between the theoretical planar and spherical sheath evolution for various densities.

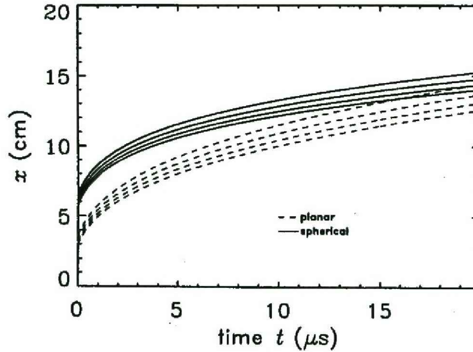

Figure B.2: A comparison of planar and spherical sheath evolution. Plots are densities (bottom to top) of 6,7,8 and 9×10^8 cm^{-3}*, whereby target potential is 20 kV and spherical target diameter is 10 cm. Taken from [Mey01].*

Appendix C

Constants and Formula

Table C.1 Physical constants

Constant	*Symbol*	*Value (SI)*
Speed of light in vacuum	c	2.998×10^{8} *m/s*
Elementary charge	e	1.602×10^{-19} *A-s*
Electron mass	m_e	9.109×10^{-31} *kg*
Atomic mass unit	m_u or *amu*	1.661×10^{-27} *kg*
Planck constant	h	6.626×10^{-34} *kg*
Boltzmann constant	k	1.381×10^{23} *J/K*
Permeability of vacuum	μ_0	$4\pi \times 10^{-7}$ *V-s/A-m*
Permittivity of vacuum	ε_0	8.854×10^{-12} *A-s/V-m*

Table C.2 Lengths

Electron Debye length $\lambda_D = \left(\frac{\varepsilon_0 k T_e}{e^2 n_e}\right) \approx 69\sqrt{\frac{T_e}{n_e}}$ λ_D *in* m, T_e *in* K, n_e *in* m^{-3}

Larmor radius $r_L = \frac{v_\perp}{\omega_c} = \frac{m v_\perp}{Z_e B}$ r_L *in* m, $v_\perp$ *in* m/s, ω_c *in* s^{-1}, e *in* $A-s$, B *in* T

Mean free path of electrons $\lambda_e = \left(\sum_\alpha n_\alpha \sigma_{e\alpha}\right)^{-1}$ λ_e *in* m, n_α *in* m^{-3}, $\sigma_{e\alpha}$ *in* m^2 *(cross section of electron collisions with particles of type* α*)*

in a slightly ionized plasma

Mean free of ions in a slightly $\lambda_i = \left(\sqrt{2n_a}\,\sigma_{ia} + \sqrt{\frac{m_i}{m_e}}\, n_e \sigma_{ie}\right)^{-1}$ λ_i *in* m, n_a *and* n_e *in* m^{-3}, σ_{ia} *and* σ_{ie} *in* m^2 *(cross section of ion collisions with atoms and electrons respectively)*

ionized plasma

Mean free path of electrons in a fully ionized plasma	$\lambda_{ei} = \frac{96\pi^3 (kT_e)^2}{Z^2 e^4 n_i \ln\Lambda} \approx \frac{1.7\times10^8 T_e^2}{Zn_i}$	λ_{ei} in m, Z mean ion charge state, T_e in K, n_i in m^{-3}, $\ln\Lambda \approx 10$ Coulomb logarithm
Width of ion matrix sheath (voltage U, initial ion density n_i)	$S_m = \left(\frac{2\varepsilon_0 U}{en_i}\right)^{1/2} \approx \sqrt{\frac{2U}{kT_e}}\lambda_D$	S_m in m, U in V, n_i in m^{-3}
Width of Child law Sheath	$S_c = \sqrt{\frac{2}{3}}\left(\frac{2U}{kT_e}\right)^{3/4}\lambda_D$	S_c in m, U in V, T_e in K

Table C.3 Frequencies

Electron plasma frequency	$\omega_{pe} = \left(\frac{\varepsilon_0 e^2 n_e}{m_e}\right)^{1/2} \approx 56.4\sqrt{n_e}$	ω_{pe} in s^{-1}, n_e in m^{-3}
Ion plasma frequency	$\omega_{pi} = \left(\frac{\varepsilon_0 Z^2 e^2 n_i}{m_i}\right)^{1/2}$	ω_{pi} in s^{-1}, n_i in m^{-3}, m_i in kg, Z ion charge number
Electron gyration frequency	$\omega_{ce} \frac{eB}{m_e} = 1.76\times10^{11} B$	ω_{ce} in s^{-1}, B in T
Ion gyration frequency	$\omega_{ci} = \frac{ZeB}{m_i} = \frac{9.55\times10^7 ZB}{M}$	ω_{ci} in s^{-1}, B in T, $M = \frac{m_i}{m_u}$ (atomic mass number of ion)

Electron-ion momentum transfer collision frequency	$\nu_{ei} = \frac{Z^2 e^4 n_i \ln\Lambda}{6\sqrt{2}\pi^{3/2} m_e^{1/2} (kT_e)^{3/2}} \approx \frac{3.6\times10^{-5} Z^2 n_i}{T_e^{3/2}}$	ν_{ei} in s^{-1}, Z mean ion charge state, T_e in K, n_i in m^{-3}, $\ln\Lambda \approx 10$ Coulomb logarithm

Table C.4 Current density

Child-Langmuir law of Space-charge limited ion Current in plane geometry	$j_i = \frac{4}{9}\varepsilon_0 \left(\frac{2e}{m_i}\right)^{1/2} \frac{U^{3/2}}{S^2}$	j_i in A/m^2, m_i in kg, sheath voltage U in V, sheath width s in m

References

[Ams69] G. Amsel, D. David, La Microanalyse De L'azote Par L'Observation Directe De Réactions Nucléaires Applications, Rev. Phys. Appl.4, 383.

[And77] H.H Andersen and J.F. Ziegler, Hydrogen –stopping powers and ranges in all elements volume 1, Pergamon Press, New York, 1977.

[And80] H.H. Andersen, F. Besenbacher, P. Loftager, and W. Moller, Large-angle scattering of light ions in the weakly screened Rutherford region, Phys Rev. A 21 (1980), 1891-1901.

[Avn74] Sidney H. Avner, Introduction to physical metallurgy, 2 ed, McGraw-Hill International Book Company, 1974, pg 249.

[Bet83] G. Bertz, and G.K. Whener, Sputtering of Multi-component Materials, in Sputtering by Particle Bombardment I: Physical Sputtering of Single Element Solids, R. Behrisch, ed., Topics in Applied Physics Vol. 47 (Springer-Verlag, Berlin) ,11-90.

[Bog02] Annemie Bogaerts, Erik Neyts, Renaat Gijbels, Joost van der Mullen, Gas discharge plasmas and their applications, Spectrochimica Acta Part B 57 (2002), 609-658.

[Boz93] Michael Bozoian, A useful formula for departures from Rutherford backscattering, Nucl. Instr. Meth. B 82 (1993), 602-603.

[Bri02] Boris Briehl and Herbert M Urbassek, Plasma recovery in plasma immersion ion implantation: dependence on pulse frequency and duty cycle, J. Phys. D: Appl. Phys. 35 (2002), 462-467.

[Che91] A. Chen, J.T. Schener, C. Ritter, R.B Alexander and J.R Conrad, Comparison between conventional and plasma source ion-implanted femoral knee components, J Appl. Phys. 70(11), 1991, 6757-6760.

[Chi11] C.D. Child, Discharge from hot CaO, Phys. Rev. 32, (1911), 492-511.

[Chu02] P.K Chu, J.Y. Chen, L.P Wang, N. Huang, Plasma-surface modification of biomaterials, Materials Science and Engineering, R36, (2002), Pg 144.

[Chu78] Wei-Kan Chu, James W. Mayer, Marc-A. Nicolet, Backscattering Spectroscopy, Harcourt Brace Jovanovich Publishers, (1978).

[Con87] J.R. Conrad, J.L. Radtke, R.A Dodd, F.J Worzala, N.C. Tran, Plasma source ion implantation technique for surface modification of materials, J. Appl. Phys. 62 (1987), 4591-4596.

[Con89] J.R. Conrad, S. Baumann, R. Fleming, and G.P. Meeker, Plasma source ion implantation dose uniformity of a 2x2 array of spherical targets, J. Appl. Phys. 65 (4), 15 February (1989), 1707-1712.

[deV99] Dawid de Villiers, Measurement of the dose rate received from low energy x-rays, produced from a plasma source, using E-PERM electrets. Internal report, National Accelerator Center, 01 August 2000.

[Fun00] A. André, Fundamentals of plasma immersion ion implantation and Deposition, John Wiley & Sons, Inc. © 2000, Pg 263.

[Hart96] J. Hartmann, W. Ensinger, R.W. Thomae, H. Bender, A Königer, B Stritzker, B Rauschenbach, Lateral implantation dose measurements of plasma immersion ion implanted non-planar samples, Nucl. Instr. and Meth. B 112 (1996), 255-258.

[Kit76] C.Kittel, Introduction to solid state physics, 5th ed, Wiley, New York, 1976.

[Lan23] I. Langmuir, The effects of Space Charge and Initial Velocities on the Potential Distribution and Thermionic Current between Parallel Plane Electrodes, Phys. Rev 21, (1923), 4.

[Lec79] J. L'Ecuyer, J.A. Davies and N. Matsunami, How accurate are aboslute Rutherford Backscattering yields, Nucl. Instr. and Meth. 160 (1979), 337-346.

[Lie89] M.A. Lieberman, Model of plasma immersion ion implantation, J. Appl. Phys. 66 (1989).

[Liz02] Lizhen Tan, J. Bauer, Wendy C. Crone, R.M Albrecht, Biocompatibility improvement of NiTi with a functionally Graded Surface, Society for experimental mechanics, 2002 SEM Annual Conference Proceedings, Milwaukee, WI, 2002.

[Mah94] Maher l. Boulos, Pierre Fauchais, and Emil Pfender, Thermal Plasmas: fundamentals and Applications, © 1994 Pleum Press, New York, Pg 177.

[May86] Leonard C. Feldman, James W. Mayer. Fundamentals of surface and thin film analysis, Elsevier Science Publishing Co.Inc, 1986, Pg 73.

[Mat84] N. Matsunami, Y. Yamamura, Y. Itikawa, N. Itoh, Y. Kazumata, S. Miyagawa, K. Morita, R. Shimizu, and H. Tawara, Energy dependence of the ion-induced sputtering yields of monoatomic solids, Atomic data and nuclear data tables, vol 31, Academic Press, New york, 1984.

[Mat94] J.N Matossian, Plasma ion implantation technology at Hughes Research Laboratories, J.Vac.Sci Technol, B 12, (1994), No 2, 850-853.

[Mey96] K.A Meyer, Two-dimensional plasma sheath observations in Plasma Source Ion Implantation, Master's thesis, University of Natal, Durban, 1996.

[Mey01] K.A Meyer, PhD Thesis, Development of a plasma source ion implantation for the modification of materials' surface, Dept of Physics, faculty of Science UCT, (2001),

[Nas96] M. Nastasi, J.W. Mayer, J.K. Hirvonen, Ion-Solid interactions Fundamentals and Applications, Cambridge University press, (1996), Pg 2,7,11.

[Pre88] R. Pretorious, J. W. Mayer and M. Peisach, Hydrogen and deuterium depth profiling by elastic recoil detection analysis, Nucl. Instr. Meth. B 35, (1988), 478-483.

[Pro94] V.M Prozesky, J.L Campbell, W.J Teesdale, J.A Maxwell, Thickness measurements of titanium nitride layers on steel using PIXE and proton backscattering, Nucl. Instru. and Meth. B 85 (1994). 108-111.

[Sch90] J.T Scheuer, N. Shamim, and J.R. Conrad, Model of plasma source ion implantation in planar, cylindrical and spherical geometries, J. Appl. Phys. 63, (1990), no 3, 1241-1245.

[Sha99] M.M. Shamim, J.T. Scheuer, R.P. Fetherston, and J.R Conrad, Measurements of emission due to ion implantation, J. Appl. Phys. 70 (9), 1 November 1999, 4756-4759.

[SIMNRA] Matej Mayer, Max- Planck Institut fur Plasmaphysik, http://www.rzg.mpg.de/~mam/, version 5.0, April 2002.

[SRIM00] J.F. Ziegler, J.P. Biersack, The Stopping and Range of Ions in Matter, Version 2000.xx , Jan. 1, 2000.

[Win70] K.B. Winterbon, P. Sigmund, and J.B. Sanders, Spatial Distributionss of Energy Deposited by Atomic Particles in Elastic Collisions, Mat. Fys. Medd. Dan Vid. Selsk. 37 (1970), no. 14,1-73.

[Wit85] A. Wittkower, J.K. Hirvonen, Some practical aspects of ion implantation for reduction, Nucl. Instr. and Meth. B 6, (1985), 78-87.

[WWW1] http://www.efunda.com/processes/surface/special.cfm

[WWW2] http://silver.neep.wisc.edu/psii/intro.htm

[WWW3] http:// www.sputtek.com/bb-comparison.html

[WWW4] http://networking.webopedia.com/TERM/B/BNC_connector.html

[Xia93] Z. Xia and C. Chan, Modelling and experiment on plasma source ion implantation, J. Appl. Phys. 73 (1993), no. 8, 3651-3656.

[Yam89] Y.Yamamura and N. Itoh, Sputtering yield, Ion Beam Assisted film Growth, (T.Itoh ed), Elsevier, Amsterdam, (1989).

[Tes95] J.R. Tesmer and M. Nastasi, Handbook of Modern Ion Beam Materials Analysis, MRS, Pittsburgh, 1995.

[Zie85] J.F. Ziegler, J.P. Biersack and U. Littmark, The stopping and range of ions in solids, the stopping and Ranges of Ions in Matter, no. 1, Pergamon Press, New York, (1985).

[Zen99] Z.M. Zeng, T.K Kwok, X.B Tian, B.Y Tang and P.K Chu, Investigation of dose uniformity on the inner races of bearings treated by plasma immersion ion implantation, J. Appl. Phys, Vol 86, No 1, (1 July 1999), 120-123.